Cell Reports

Article

Neutrophil-inflicted vasculature damage suppresses immune-mediated optic nerve regeneration

Graphical abstract

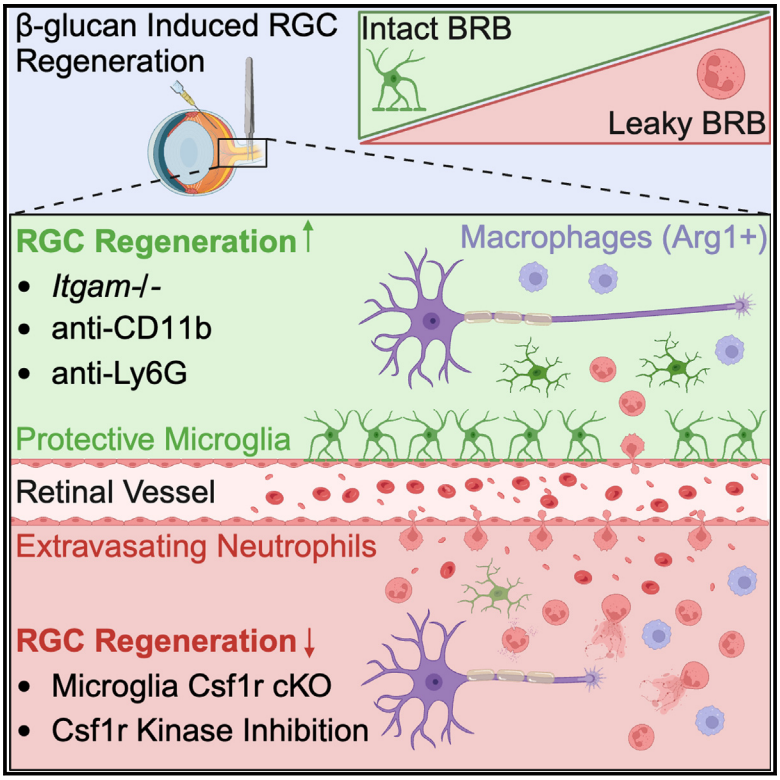

Highlights

- Intra-ocular injection of highly purified β-glucan promotes RGC axon regeneration
- Intra-ocular β-glucan causes vascular inflammation and BRB leakiness
- Ablation of microglia increases BRB leakiness and attenuates RGC regeneration
- Acute blocking of Ly6G^{+} neutrophils protects the BRB and enhances RGC regeneration

Authors

Ryan Passino, Matthew C. Finneran, Hannah Hafner, ..., Daniel H. Geschwind, Larry I. Benowitz, Roman J. Giger

Correspondence

rgiger@umich.edu

In brief

Passino et al. demonstrate that retinal ganglion cell (RGC) axon regeneration, triggered by intra-ocular β-glucan administration, is enhanced by manipulations that reduce vascular inflammation and protect the blood-retina barrier (BRB). They show that perivascular microglia protect the BRB, whereas pro-inflammatory neutrophils increase BRB leakiness and reduce RGC regeneration.

Passino et al., 2024, Cell Reports *43*, 113931
March 26, 2024
https://doi.org/10.1016/j.celrep.2024.113931

CellPress

Cell Reports

CellPress
OPEN ACCESS

Article

Neutrophil-inflicted vasculature damage suppresses immune-mediated optic nerve regeneration

Ryan Passino,[1] Matthew C. Finneran,[1,2,13] Hannah Hafner,[1,13] Qian Feng,[1] Lucas D. Huffman,[1,2] Xiao-Feng Zhao,[1] Craig N. Johnson,[1] Riki Kawaguchi,[3,5,12] Juan A. Oses-Prieto,[4] Alma L. Burlingame,[4] Daniel H. Geschwind,[3,5,6,8] Larry I. Benowitz,[9,10,11] and Roman J. Giger[1,2,7,14,*]

[1]Department of Cell and Developmental Biology, University of Michigan Medical School, Ann Arbor, MI 48109, USA
[2]Neuroscience Graduate Program, University of Michigan Medical School, Ann Arbor, MI 48109, USA
[3]Departments of Psychiatry and Neurology, University of California, Los Angeles, Los Angeles, CA 90095, USA
[4]University of California San Francisco, Department of Pharmaceutical Chemistry, San Francisco, CA 94158, USA
[5]Program in Neurogenetics, David Geffen School of Medicine, University of California, Los Angeles, Los Angeles, CA 90095, USA
[6]Department of Human Genetics, David Geffen School of Medicine, University of California, Los Angeles, Los Angeles, CA 90095, USA
[7]Department of Neurology, University of Michigan Medical School, Ann Arbor, MI 48109, USA
[8]Institute of Precision Health, University of California, Los Angeles, Los Angeles, CA 90095, USA
[9]Departments of Neurosurgery and Ophthalmology, Harvard Medical School, Boston, MA 02115, USA
[10]Department of Neurosurgery, Boston Children's Hospital, Boston MA 02115, USA
[11]Departmant of Ophthalmology, University of Pittsburgh Medical Center, Pittsburgh, PA 15213, USA
[12]Center for Neurobehavioral Genetics, Semel Institute for Neuroscience and Human Behavior, University of California, Los Angeles, Los Angeles, CA 90095, USA
[13]These authors contributed equally
[14]Lead contact
*Correspondence: rgiger@umich.edu
https://doi.org/10.1016/j.celrep.2024.113931

SUMMARY

In adult mammals, injured retinal ganglion cells (RGCs) fail to spontaneously regrow severed axons, resulting in permanent visual deficits. Robust axon growth, however, is observed after intra-ocular injection of particulate β-glucan isolated from yeast. Blood-borne myeloid cells rapidly respond to β-glucan, releasing numerous pro-regenerative factors. Unfortunately, the pro-regenerative effects are undermined by retinal damage inflicted by an overactive immune system. Here, we demonstrate that protection of the inflamed vasculature promotes immune-mediated RGC regeneration. In the absence of microglia, leakiness of the blood-retina barrier increases, pro-inflammatory neutrophils are elevated, and RGC regeneration is reduced. Functional ablation of the complement receptor 3 (CD11b/integrin-αM), but not the complement components *C1q*$^{-/-}$ or *C3*$^{-/-}$, reduces ocular inflammation, protects the blood-retina barrier, and enhances RGC regeneration. Selective targeting of neutrophils with anti-Ly6G does not increase axogenic neutrophils but protects the blood-retina barrier and enhances RGC regeneration. Together, these findings reveal that protection of the inflamed vasculature promotes neuronal regeneration.

INTRODUCTION

Trauma, stroke, and neurodegenerative disorders can result in irreversible damage to the central nervous system (CNS), leading to permanent neurological deficits. CNS injury is typically accompanied by a robust inflammatory response, characterized by microgliosis and astrogliosis, and, depending on the severity, by infiltration of hematogenous immune cells. CNS inflammation can have both beneficial effects, helping to mitigate damage and promote repair, and detrimental effects, including collateral damage, exacerbating tissue harm. In preclinical studies, experimental manipulation of injury-induced inflammation has shown promise in improving axonal regeneration and neural repair.[1–7]

Retro-orbital optic nerve crush (ONC) injury in mice is a powerful experimental model for studying the response of CNS neurons to trauma. Retinal ganglion cells (RGCs), the projection neurons in the retina, send axons through optic nerves and tracts to transmit visual information to the brain. ONC triggers microglial activation and leads to the secretion of cytokines in the retina that contribute to the demise of injured RGCs.[8,9] However, the role of microglia in the injured visual system remains a topic of debate, and depending on context, microglia can either be detrimental or protective.[10–13] In cases of stroke or CNS trauma, depleting microglia has been shown to result in worse functional outcomes,[14–17] but see also Hilla et al.[11] and Willis et al.[18] Data interpretation following microglial ablation is challenging because of their diverse roles in inflammation, phagocytosis of pathogens and damaged cells,[19] activity-dependent synaptic pruning,[20] and regulation of vascular tone, as well as protection of the blood-brain barrier and neurovascular unit.[21–26]

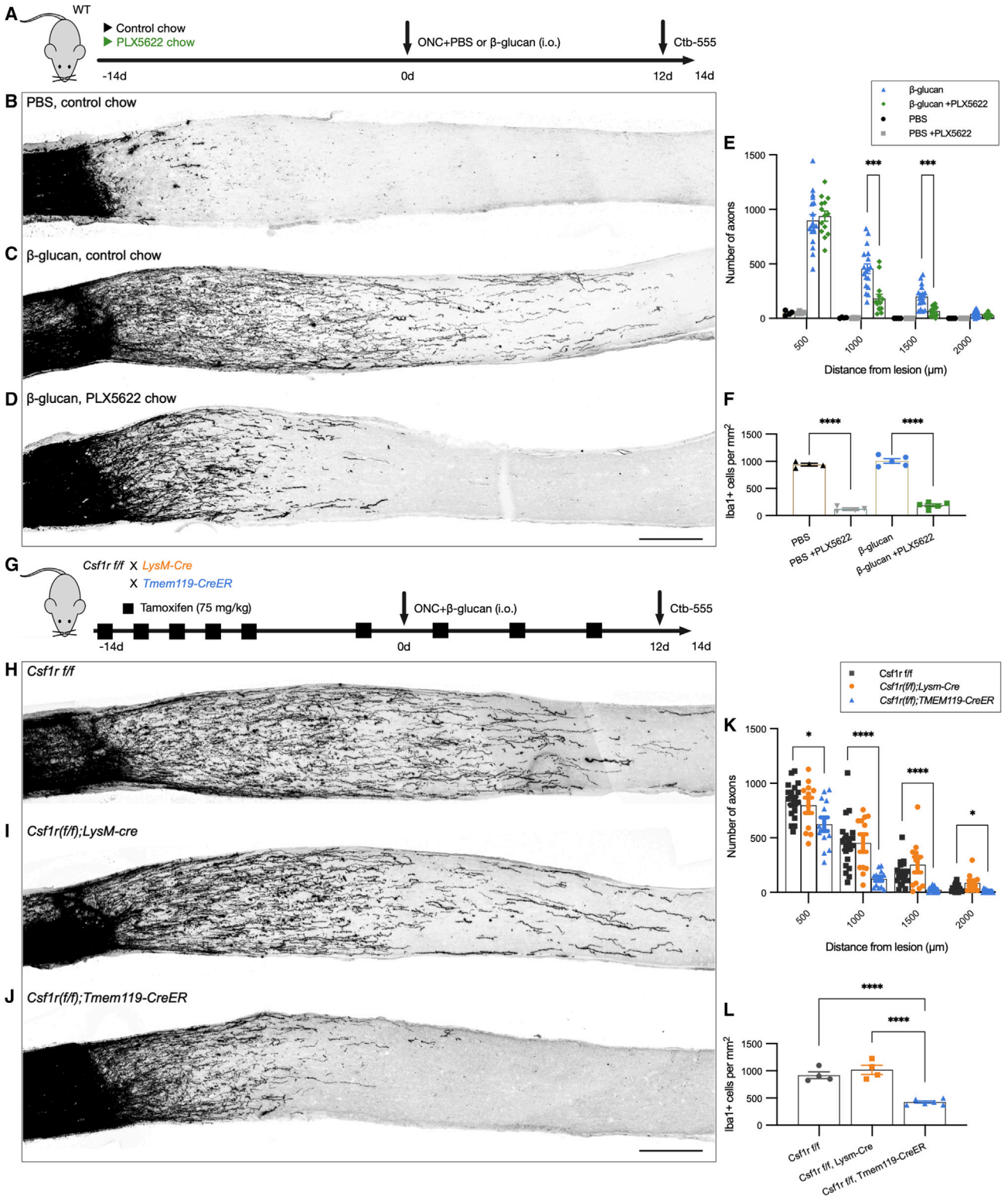

Figure 1. Microglia ablation attenuates immune-mediated RGC axon regeneration

(A) Experimental timeline of optic nerve regeneration in PLX5622-fed mice.

(B–D) CTB-traced axons at 14 dpc plus i.o. (B) PBS, (C) β-glucan, and (D) β-glucan on PLX5622 chow. Scale bar, 200 μm.

(legend continued on next page)

In the visual system, manipulating the immune milieu in the vitreous humor can greatly influence RGC survival and axon regeneration following ONC.[27] For instance, intra-ocular (i.o.) injection of zymosan, a crude yeast cell wall extract that acts as a pathogen-associated molecular pattern (PAMP), induces a strong inflammatory response that promotes RGC growth and leads to extensive axon regeneration,[28] and this effect can be exceeded by injecting a population of immature neutrophils.[29] In stark contrast, inflammation triggered by i.o. lipopolysaccharide fails to stimulate RGC axon regeneration.[30] Mechanistic studies identified particulate β-glucan as the active ingredient in zymosan, responsible for RGC regeneration through the engagement of diverse pattern recognition receptors on myeloid cells, including Toll-like receptor 2 and dectin-1.[30] Monocytes (Mos), macrophages (Macs), and neutrophils that accumulate in the vitreous have been studied extensively and shown to contribute to immune-mediated RGC regeneration.[28–32] This work resulted in the identification of numerous pro-regenerative molecules released by ocular immune cells.[28,31,33–35] Yet, despite the strong pro-regenerative and neuroprotective effects of the identified immune molecules, reports of bystander toxicity exist[30,36] and undermine the beneficial effects of immune-mediated neurorepair.

Here, to distinguish between the beneficial and detrimental effects of ocular inflammation toward injured RGCs, we investigated the roles of specific immune cell types. We show that ocular inflammation induced by β-glucan mobilizes large numbers of conventional neutrophils that cause vascular damage and increase permeability of the blood-retina barrier (BRB). Mechanistically, experimental manipulations that increase vascular inflammation and BRB permeability diminish RGC axon regeneration, whereas interventions that reduce vascular inflammation and protect the BRB strongly enhance RGC regeneration. Our study demonstrates that beneficial and detrimental effects associated with β-glucan-elicited inflammation can be assigned to specific innate immune cell populations and that damage to the microvasculature is a major obstacle to CNS regeneration.

RESULTS

Particulate, but not soluble, β-(1,3)(1,6)-glucan promotes axon regeneration

Crude preparations of β-glucans, including zymosan and curdlan, are known to promote regeneration of injured RGCs upon i.o. injection.[28,30] Due to the variable regenerative outcomes associated with different batches of zymosan and the known detrimental effects such as retinal microhemorrhage and detachment,[30] we sought to determine whether highly purified β-glucans extracted from *S. cerevisiae* exhibit superior effects, namely enhanced axon regeneration with simultaneous reduction of adverse effects. β-Glucans are PAMPs, and both particulate (insoluble) and soluble forms elicit strong immune responses. However, particulate and soluble β-glucans from *S. cerevisiae* elicit distinct immune responses,[37] and therefore we tested β-(1,3)(1,6)-glucans in particulate [IRI-1501] and soluble [IRI-1800] forms (Figures S1A–S1D). Only particulate, but not soluble, β(1,3)(1,6)-glucan elicited RGC regeneration upon i.o. injection (Figure S1E). Although axon regeneration achieved with particulate β-(1,3)(1,6)-glucan (hereafter β-glucan) was more robust than with zymosan (Figure S1E), both compounds are associated with undesirable side effects, including retinal detachment (Figures S1F–S1I).[30] We conclude that retinal toxicity is not caused by impurities in different β-glucan preparations but rather is an inherent feature of β-glucan-elicited inflammation. This observation prompted further investigations into the underlying cellular and molecular phenomena.

Pharmacological and genetic ablation of microglia attenuates immune-mediated RGC axon regeneration

To examine whether microglia are beneficial or detrimental for immune-mediated RGC axon regeneration, cohorts of mice were treated for 2 weeks with control chow or chow containing the Csf1R inhibitor PLX5622 to pharmacologically ablate microglia, after which they were subjected to ONC and i.o. β-glucan or physiological saline (vehicle) injection. Mice were maintained on PLX5622 chow until they were sacrificed at 14 days post-crush (dpc). Regenerated axons were labeled by i.o. injection of a cholera toxin beta subunit (CTB-555) (Figure 1A). The length and number of axons that regenerated beyond the nerve crush site were assessed in longitudinal optic nerve sections. For unbiased quantification, we wrote code for automated tracing and quantification of axons at different distances from the injury site (see STAR Methods). In PLX5622-fed mice, β-glucan-elicited RGC axon regeneration was partially yet significantly reduced (Figures 1B–1E). The efficiency of microglia ablation was assessed by anti-Iba1 immunofluorescence labeling (Figures 1F and S2A–2E). Although a subpopulation of microglia persists in PLX5622-fed mice,[38] we found a ~90% reduction in optic nerves and tracts.[11,38,39] Together, our studies indicate that

(E) Quantification of regenerated axons at 14 dpc (y axis) at different distances (x axis) from crush site. i.o. PBS (n = 4 nerves); i.o. PBS and PLX5622 (n = 4); i.o. β-glucan (n = 18); i.o. β-glucan and PLX5622 (n = 14). Results are presented as mean ± SEM. Data were analyzed with two-way ANOVA followed by Tukey's multiple comparisons. ***$p \leq 0.001$.

(F) Quantification of Iba1$^+$ cells per mm^2 in optic nerve sections, 14 dpc. n = 4–5 nerves per group, one-way ANOVA followed by Tukey's multiple comparisons. ****$p \leq 0.0001$.

(G) Experimental timeline of optic nerve regeneration in *Csf1r* conditional mutants.

(H–J) CTB-traced axons at 14 dpc plus i.o. β-glucan in (H) *Csf1rf/f* (n = 19 nerves), (I) *Csf1r f/f;LysM-Cre* (n = 11), and (J) *Csf1r f/f;Tmem119-CreER* (n = 13) mice. Scale bar, 200 μm.

(K) Quantification of regenerated axons at 14 dpc. Results are presented as mean ± SEM. Data were analyzed with two-way ANOVA followed by Tukey's multiple comparisons. *$p \leq 0.05$ and ****$p \leq 0.0001$.

(L) Quantification of Iba1$^+$ cells per mm^2 in optic nerve sections, 14 dpc. n = 4–6 nerves per group, analyzed with one-way ANOVA followed by Tukey's multiple comparisons. ****$p \leq 0.0001$.

See also Figures S1 and S2.

pharmacological ablation of microglia attenuates β-glucan-mediated RGC repair.

Because Csf1R is not only expressed by microglia but also by blood-borne immune cells,[40] we employed conditional gene ablation in *Csf1r(f/f)* mice to further dissect the roles of select immune populations. For gene deletion in Mos/Macs, we generated *Csf1r(f/f);LysM-cre* mice. For acute deletion in microglia, we generated *Csf1r(f/f);Tmem119-creER* mice and treated mice with tamoxifen. Control *Csf1r(f/f)* mice were subjected to the same tamoxifen regimen. Next, mice were subjected to ONC plus i.o. β-glucan, and 2 weeks later, optic nerves were harvested and sectioned, and regenerated axons were quantified (Figure 1G). Deletion of *Csf1r* in Mos/Macs resulted in lengthy RGC axon regeneration, comparable to parallel-processed *Csf1r(f/f)* littermate controls (Figures 1H, 1I, and 1K). However, inducible *Csf1r* ablation in microglia significantly reduced axon regeneration, comparable to PLX5622-fed mice (Figures 1J and 1K). Cre recombination efficiency was demonstrated in parallel-processed *LysM-cre* and *Tmem119-creER* mice crossed onto a *ROSA26-EGFP* background (Figure S2). To confirm microglial ablation, optic nerve sections were stained with anti-Iba1. *Csf1r(f/f);Tmem119-creER* mice display a significant (60% ± 4%), yet incomplete, reduction in Iba1$^+$ cells when compared to *Csf1r(f/f)* littermates and *Csf1r(f/f);LysM-cre* mice (Figure 1L). Collectively, these studies suggest that microglia are important for full-blown immune-mediated RGC axon regeneration and that *Csf1r* in Mos/Macs is dispensable.

Following optic nerve injury, microglia protect the BRB

Following retro-orbital ONC, retinal microglia are rapidly activated and shape the retinal immune milieu.[41] To assess microglia morphological changes upon ONC, we prepared retinal flat mounts from wild-type (WT) and *Tmem119-EGFP* reporter mice for immunofluorescent staining with anti-CD31 and anti-Iba1 to visualize the retinal microvasculature and microglia (Figures 2 and S3). In naive retina, microglia are highly ramified and show tiling (Figure 2A). At 1 dpc injury to the optic nerve, perivascular microglia in the inner retina move closer to microvessels, aligning their processes to envelope vessels. Quantification reveled a significant increase in microglia exhibiting an "enveloping" behavior upon ONC (Figures 2B–2E, S3A, and S3B). Of note, ONC causes vascular damage resulting in increased BRB leakiness at 3 dpc (Figure S3C). Because microglia play an important role in blood-brain-barrier integrity[21,25,42–44] and protect against vascular damage,[45] we assessed ONC-inflicted BRB leakiness in the presence or absence of microglia. In PLX5622-fed mice, greater than 90% of retinal microglia were lost (Figure 2D). In naive mice, BRB leakiness was minimal and was not significantly altered in the absence of microglia. However, at 3 days following ONC, BRB leakiness was increased and exacerbated in the absence of microglia (Figure 2F). To assess the impact of microglial ablation on RGC viability following ONC, retinal flat mounts were stained with anti-RBPMS. At 14 dpc, mice on control chow and PLX5622-fed mice showed 82% ± 1% and 82% ± 2% reductions in RGCs, respectively (Figure 2G). These studies show that perivascular microglia in the retina rapidly respond to ONC and that microglia help to protect BRB integrity but not survival of axotomized RGCs.

Microglia reduce accumulation of hematogenous immune cells in the eye

Immune cells can enter the eye through the retinal vasculature or the choroid and rapidly accumulate in the vitreous.[46–48] To investigate how loss of microglia may influence ocular inflammation, we separately analyzed the vitreous and retinas using flow cytometry. The gating scheme is shown in Figure S4A. Eyes were injected with β-glucan, and at 3 and 7 dpc, vitreous and retinas were harvested and analyzed separately. Experimental groups included *Csf1r(f/f)* mice fed with control chow or PLX5622 chow and *Csf1r(f/f);Tmem119-CreER* mice fed with control chow. All mice received tamoxifen treatment as indicated (Figure 3A). In both the retinas and vitreous, neutrophils and Mos/Macs are the most abundant immune cell types.[30,31] Compared to 3 dpc mice on control chow, the vitreous of PLX5622-fed mice showed a significant increase in myeloid cells, including neutrophils (Ly6G$^+$) and Macs (Ly6C^{int} and Ly6C$^-$) but not Mos (Ly6C^{hi}) (Figures 3B–3D). In *Csf1r(f/f);Tmem119-creER* mice at 3 dpc, neutrophils, but not Macs, were significantly increased (Figures 3B–3D). At 7 dpc, neutrophils remained significantly elevated in PLX5622-fed and *Csf1r(f/f);Tmem119-creER* mice, and there was a significant increase in Macs in *Csf1r(f/f);Tmem119-creER* mice (Figures 3E–3G). In parallel-processed retinas, inflammation was not significantly altered in the absence of microglia (Figures 3H–3M). Together, these studies indicate that microglia protect the eye from excessive inflammation following i.o. β-glucan administration.

To investigate the route of entry for neutrophils that accumulate in the vitreous, we employed *Catchup* reporter mice. In *Catchup* mice, *Ly6g-cre*-mediated recombination of *ROSA26-tdTomato* (tdT) allows linage tracing of granulocytes (GCs; mainly neutrophils).[49,50] To assess the percentile of Ly6G$^+$ neutrophils that are tdT$^+$ in heterozygous *Catchup* mice (*Catchup*$^{+/-}$), we carried out flow cytometry of circulating blood and spleen cells. The gating scheme is shown in Figures S4B–S4S. We find that 95% and 93% of tdT$^+$ cells show surface Ly6G staining and that 72% and 66% of Ly6G$^+$ neutrophils express tdT in blood and spleen, respectively (Figures S4D, S4M, S4J, and S4S). Blood supply to the retina is provided by a prominent vessel that runs through the optic nerve and, upon entry into the retina, branches into several arterioles that run toward the retinal periphery. Capillary blood drains into post-capillary venules and exits the eye through the optic nerve vein.[51] We harvested retinas from naive and 1 dpc *Catchup*$^{+/-}$ mice for flat-mount staining of blood vessels with anti-CD31 (Figure 3N). Whereas very few neutrophils were detected in naive retinas, we observed a small increase in the vasculature of the inner retina at 1 dpc with i.o. PBS (Figures S5A and S5B). Quite strikingly, at 1 dpc with i.o. β-glucan, there was a massive increase in neutrophils in the inner retina (Figure 3O), with noticeable damage to the microvasculature (Figure S5C). Neutrophils were prominently found within post-capillary venules and the perivascular space. In PLX5622-fed mice, there was a further increase in extravascular neutrophils (Figure 3P). Neutrophils were largely absent from retinal arterioles and capillary, underscoring preferential extravasation and entry into the eye through post-capillary venules.[52] These experiments show that i.o. β-glucan causes severe retinal vasculitis and that the presence of microglia attenuates accumulation of neutrophils.

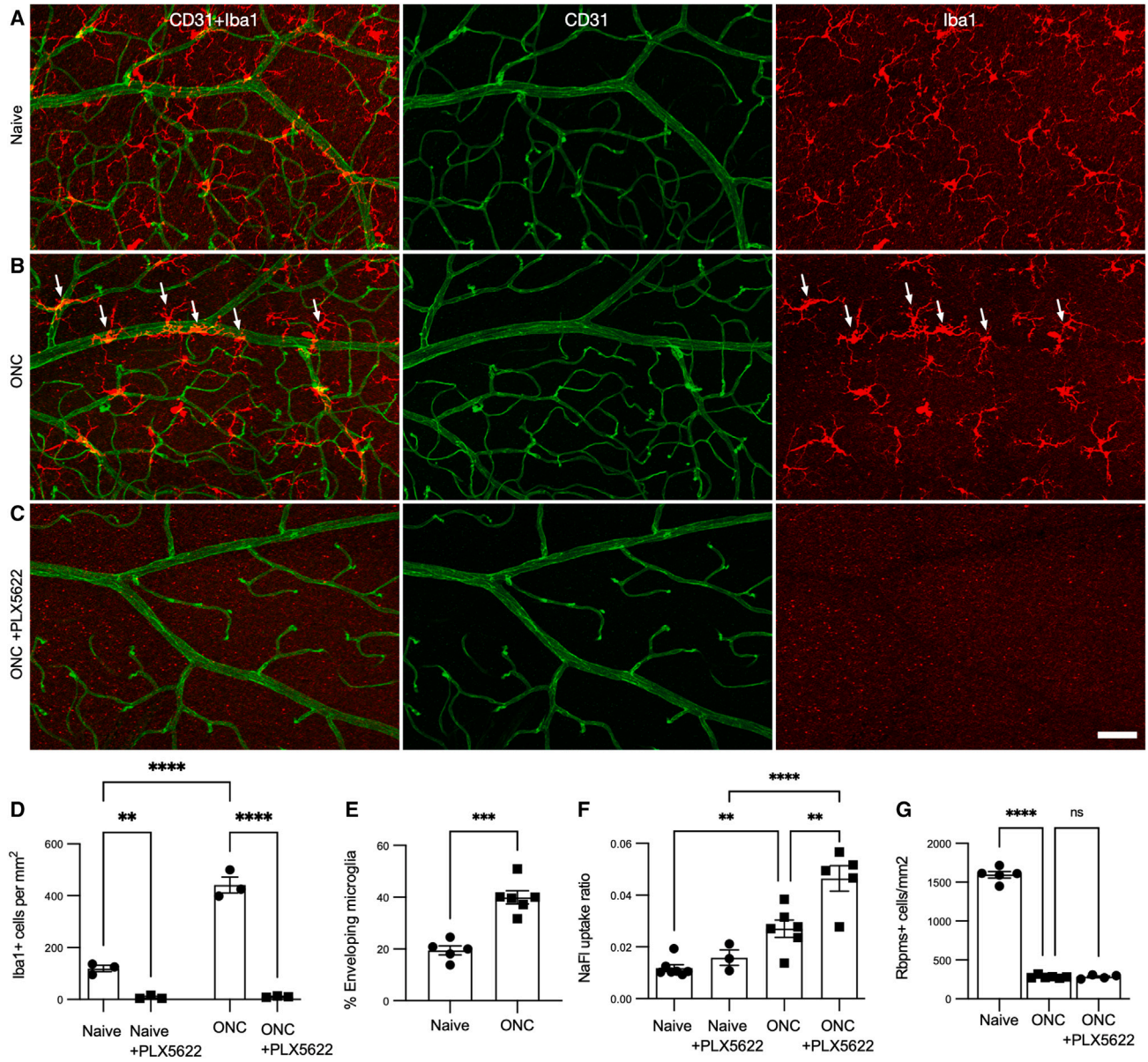

Figure 2. Microglia protect the blood-retina barrier following optic nerve injury

(A–C) Retinal flat mounts stained with anti-CD31 and anti-Iba1 from naive and 1 dpc controls and PLX5622-fed mice. Arrowheads mark perivascular, enveloping microglia. Scale bar, 50 μm.

(D) Quantification of microglia ablation. y axis, Iba1^{+} cells per mm^{2}. Results are presented as mean ± SEM. Student's t test. **p ≤ 0.01 and ****p ≤ 0.0001.

(E) Enveloping microglia in naive (n = 5) and 1 dpc (n = 6) retinas. Results are presented as mean ± SEM. Student's t test. ***p ≤ 0.001.

(F) Quantification of BRB leakiness. NaFL entry into the retina, normalized to NaFL in blood. y axis, uptake ratio. N = 3–7 per group (2 retinas each). Data were analyzed with one-way ANOVA followed by Tukey's multiple comparisons. **p ≤ 0.01 and ****p ≤ 0.0001.

(G) Quantification of RBPMS^{+} RGCs of naive and 14 dpc mice. Results are presented as mean ± SEM. Data were analyzed with one-way ANOVA followed by Tukey's multiple comparisons. ****p ≤ 0.0001, ns, not significant.

See also Figure S3.

Loss of CD11b attenuates ocular inflammation and enhances immune-mediated axon regeneration

CD11b (integrin-αM) is known to associate with CD18 (integrin-β2) to form heterodimeric MAC-1, also known as complement receptor 3. Activated neutrophils express high levels of surface CD11b important for transendothelial migration and extravasation.[53,54] MAC-1 interacts with ICAM1 and ICAM2 on the luminal side of endothelial cells and is important for crawling along the endothelium.[53–55] Commensurate with these interactions, we observed reduced ocular inflammation in *Itgam*$^{-/-}$ mice (lacking CD11b) following i.o. β-glucan compared to parallel-processed WT mice. Flow cytometric analysis of immune cell composition

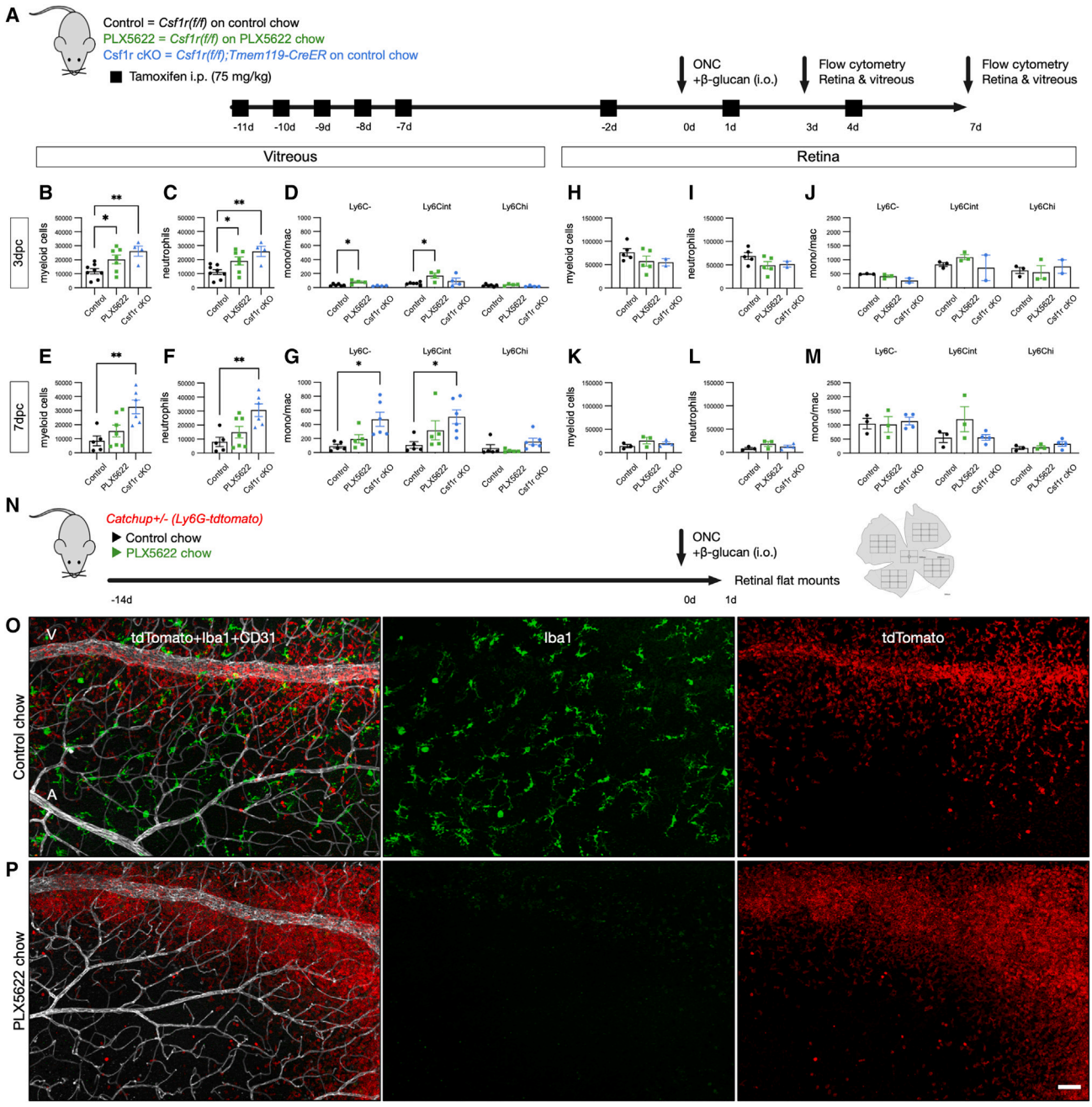

Figure 3. Microglia attenuate neutrophil accumulation in the eye and protect the inflamed vasculature

(A) Experimental timeline for assessment of myeloid cells in the vitreous and retinas of *Csf1r f/f* conditional mutants and PLX5622-fed mice.

(B–M) Quantification of immune cells by flow cytometry. Innate immune cells ($CD45^+CD11b^+$), neutrophils ($Ly6G^+$), and monocytes/macrophages ($Ly6C^-$, $Ly6C^{low}$, $Ly6C^{hi}$) in the vitreous at (B–D) 3 and (E–G) 7 dpc. Innate immune cells ($CD45^+CD11b^+$), neutrophils ($Ly6G^+$), and monocytes/macrophages ($Ly6C^-$, $Ly6C^{low}$, $Ly6C^{hi}$) in the retina at (H–J) 3 and (K–M) 7 dpc. A minimum of n = 3 per condition. Results are presented as mean ± SEM. Data were analyzed with one-way ANOVA followed by Tukey's multiple comparisons. *$p \leq 0.05$ and **$p \leq 0.01$.

(N) Experimental timeline for imaging retinal infiltration by neutrophils in *Catchup*$^{+/-}$ mice.

(O–P) Flat mounts of *Catchup* retinas at 1 dpc with i.o. β-glucan ± PLX5622. Neutrophils (red), CD31 (white), and Iba1 (green). Scale bar, 50 μm. V, venule, A, arteriole.

See also Figures S4 and S5.

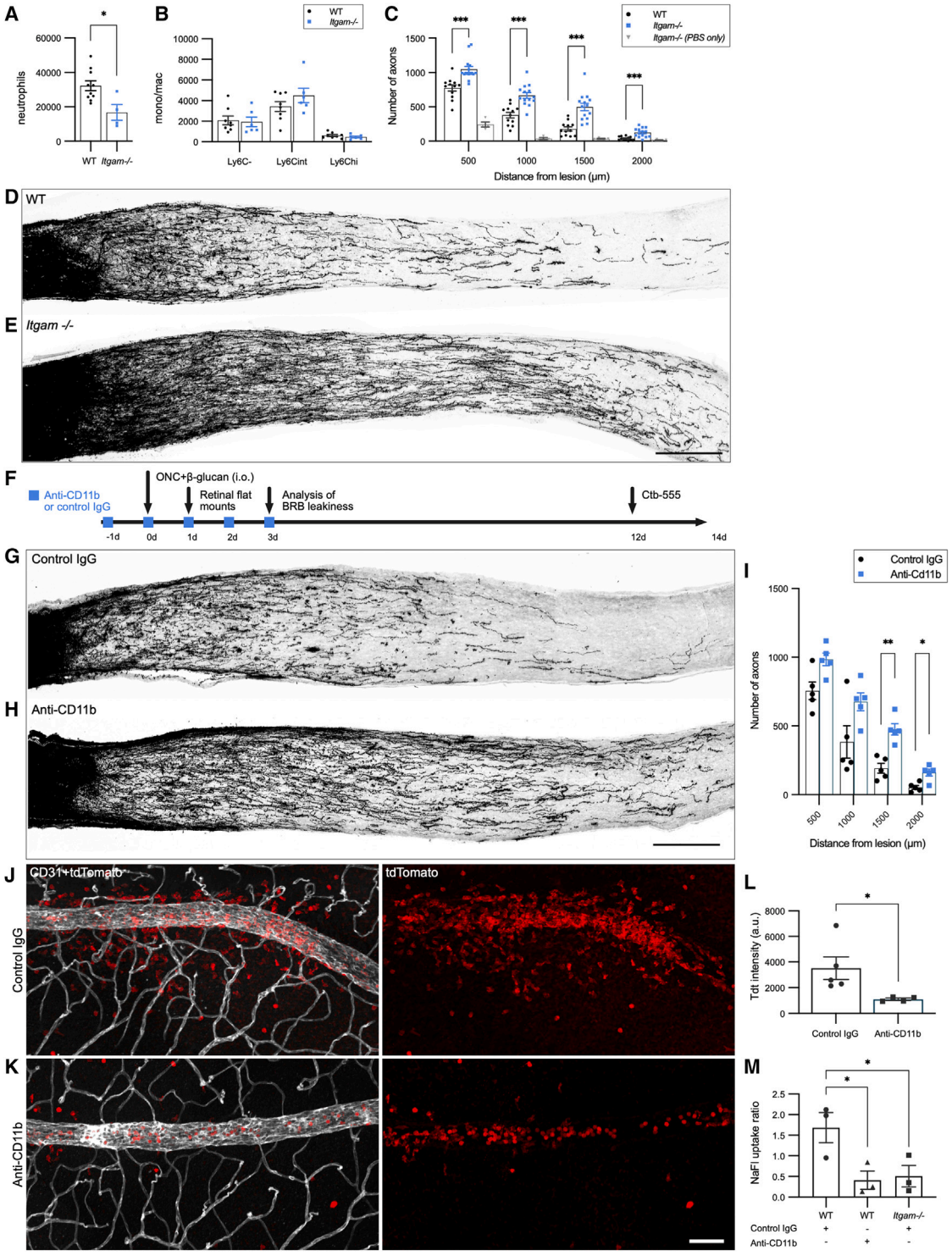

Figure 4. Loss of CD11b attenuates neutrophil recruitment and enhances immune-mediated RGC axon regeneration

(A and B) Quantification of neutrophils and macrophages in WT (n = 10) and *Itgam*$^{-/-}$ eyes (n = 4) at 3 dpc plus i.o. β-glucan. Data are presented as mean ± SEM, unpaired Student's t test. *p ≤ 0.05.

(C) Quantification of regenerated axons with β-glucan at 14 dpc (y axis) at different distances (x axis) from crush site in WT (n = 12 nerves), *Itgam*$^{-/-}$ (n = 14), and *Itgam*$^{-/-}$ plus i.o. PBS (n = 4). Results are presented as mean ± SEM. Data were analyzed with two-way ANOVA followed by Tukey's multiple comparisons. ***p ≤ 0.001.

(legend continued on next page)

in *Itgam*$^{-/-}$ eyes at 3 dpc plus i.o. β-glucan revealed a significant reduction in ocular neutrophils but not in Mos/Macs (Figures 4A and 4B).

To ask whether the reduced neutrophil accumulation in *Itgam*$^{-/-}$ mice impacts RGC regeneration, optic nerves were analyzed. Strikingly at 14 dpc, RGC axon regeneration was greatly enhanced compared to parallel-processed WT mice (Figures 4C–4E). Similar to WT mice, i.o. saline injection in *Itgam*$^{-/-}$ mice failed to elicit RGC axon regeneration (Figure 4C). Importantly, acute administration of the monoclonal anti-CD11b blocking antibody (M1/70), at 1 day prior to ONC, at the time of ONC, and daily for 3 subsequent days, also enhanced β-glucan-elicited RGC axon regeneration compared to parallel-processed mice treated with control immunoglobulin G (IgG) (Figures 4F–4I). This rules out potential confounding effects caused by germline ablation of the *Itgam* gene. Moreover, analysis of *Catchup*$^{+/-}$ mice treated with the M1/70 antibody showed a reduction in neutrophil infiltration into the eye at 1 dpc plus β-glucan (Figures 4J–4L).

The pro-regenerative effects observed upon acute or chronic CD11b/*Itgam* ablation, as seen in β-glucan-treated mice, are quite striking and prompted further investigations. Specifically, we wondered whether in a non-immune-driven RGC regeneration paradigm, such as knockdown of the tumor-suppressor phosphatase and tensin homolog (PTEN) in *Itgam*$^{-/-}$ mice, results in augmented regeneration of injured RGCs. Upon i.o. injection of adeno-associated viral vector (AAV2)-shPTEN into WT mice, enhanced RGC axon regeneration is observed at 14 dpc.[56] In parallel-processed *Itgam*$^{-/-}$ mice, subjected to AAV2-shPTEN injection followed by ONC, RGCs showed robust axon regeneration (Figures S5E and 5F). Quantification of regenerated axons revealed that the number and length are very similar between the two genotypes (Figure S5G). This demonstrates that in a non-immune-mediated RGC regeneration paradigm, ablation of *Itgam* does not result in a further increase in axon regeneration. To demonstrate that AAV2-shPTEN combined with ONC does not alter ocular inflammation, we used *Catchup*$^{+/-}$ mice and indeed found no increase in neutrophils following PTEN knockdown (Figure S5D).

Next, we examined whether functional ablation of CD11b protects the BRB upon i.o. β-glucan. This was indeed the case since in both *Itgam*$^{-/-}$ mice and M1/70-antibody-treated WT mice, leakiness of sodium fluorescein (NaFL) into retinas was significantly reduced at 3 dpc (Figure 4M). Together, these studies show that chronic or acute loss of CD11b reduces vascular inflammation, protects the BRB, and increases immune-mediated RGC axon regeneration.

β-glucan triggers accumulation of pro-inflammatory neutrophil subpopulations in WT and *Itgam*$^{-/-}$ mice

While flow cytometry of ocular immune infiltrates revealed a significant reduction in *Itgam*$^{-/-}$ neutrophils during the first week, a detailed analysis of immune profiles was hampered by the absence of CD11b (Figures 4A and 4B). As an alternative approach, we used anti-CD45 magnetic-activated cell sorting (MACS) to capture ocular immune cells in the vitreous and retinas, followed by single-cell RNA sequencing (scRNA-seq) (Figure 5A). From two runs per genotype, carried out at 3 dpc plus i.o. β-glucan, we obtained 16,666 high-quality cells from WT mice and 16,493 from *Itgam*$^{-/-}$ mice (Figure S6A). Datasets were subjected to dimensional reduction through principal-component analysis. The first 20 principal components were used for shared nearest neighbor and Louvain cluster determination with the resolution parameter set at 0.5; uniform manifold approximation and projection was used for cell cluster visualization. As expected, in both WT and *Itgam*$^{-/-}$ mice, leukocytes were the most prevalent cell type, making up ~70%. Non-immune cells included *Cnga1*$^{+}$ rod (~30%) and *Arr3*$^{+}$ cone (<1%) photoreceptors and *Cabp5*$^{+}$ bipolar cells (<1%) (Figures S6B–S6D and S6G–S6I). Non-immune cells were eliminated *in silico* prior to downstream analysis. The remaining cells were used for dataset integration together with single-cell transcriptomes of naive WT mouse peripheral blood mononuclear cells (PBMCs)[57] (Figures 5B and 5C).

Leukocytes that respond to β-glucan in WT and *Itgam*$^{-/-}$ mice primarily include *S100a8/S100a9*$^{+}$ GCs (70.5% in WT and 70.5% in *Itgam*$^{-/-}$) and are represented in clusters 1–6 (GC1–GC6) (Figures 5D–5J). Some eosinophils (*Siglecf*, ~ 5% of all GC) are found in cluster GC2, and there are very few basophils (*Ccr3*, <1%). This shows that the vast majority of GCs entering the eye upon i.o. β-glucan plus ONC are neutrophils. Mos (cluster 7) express *Ccr2* (Figures 5Q–5S) and *Ly6c2* and make up < 2% (Figures S6E and S6J). Three clusters with *Lyz2*$^{+}$ Macs (Mac1–Mac3) make up 16% of WT and 16% of *Itgam*$^{-/-}$ leukocytes (Figures 5G and S6K–S6F). Mac subpopulations express high levels of extracellular matrix molecules (*Fn1*/fibronectin, *Vim*/vimentin, syndecan/*Sdc1* and *Sdc3*) (Figures 5C and 5T–5V). Of interest, cluster 8 (Mac1) is enriched for gene products previously implicated in RGC regeneration (*Spp1/osteopontin*, *Thbs1/thrombospondin*, *Psap*/prosaposin, *Fn1*, *Inhba*/activin A, *Grn*/granulin precursor, and *Vegfa*) as well as gene products implicated in inflammation resolution (*Arg1/arginase-1*, *Hmox1*/heme oxygenase, *Lgals3*/galectin-3, and *Ccl24*) (Figure 5C). Some of the previously studied regeneration-associated molecules oncomodulin (*Ocm*), stromal-cell-derived factor-1

(D–E) CTB-traced axons at 14 dpc plus i.o. β-glucan in (D) WT and (E) *Itgam*$^{-/-}$ mice. Scale bar, 200 μm.
(F) Experimental timeline for anti-CD11b treatment.
(G and H) CTB-traced axons at 14 dpc following i.o. β-glucan and systemic (G) control IgG (n = 5 nerves) and (H) anti-CD11b (n = 5). Scale bar, 200 μm.
(I) Quantification of regenerated axons. Results are presented as mean ± SEM, analyzed with two-way ANOVA followed by Tukey's multiple comparisons. *p ≤ 0.05 and **p ≤ 0.01.
(J and K) Flat mounts of *Catchup*$^{+/-}$ retinas treated with control IgG or anti-CD11b at 1 dpc plus i.o. β-glucan, stained with anti-CD31. Scale bar, 50 μm.
(L) Quantification of neutrophils in retinas in mice treated with control IgG (n = 4), and anti-CD11b (n = 4). y axis, tdT fluorescence intensity in arbitrary units (a.u.). Data were analyzed with unpaired Student's t test. *p ≤ 0.05.
(M) Quantification of BRB leakiness. y axis shows the calculated NaFL uptake ratio (n = 3). Results are presented as mean ± SEM. Data were analyzed with one-way ANOVA followed by Tukey's multiple comparisons. *p ≤ 0.05.

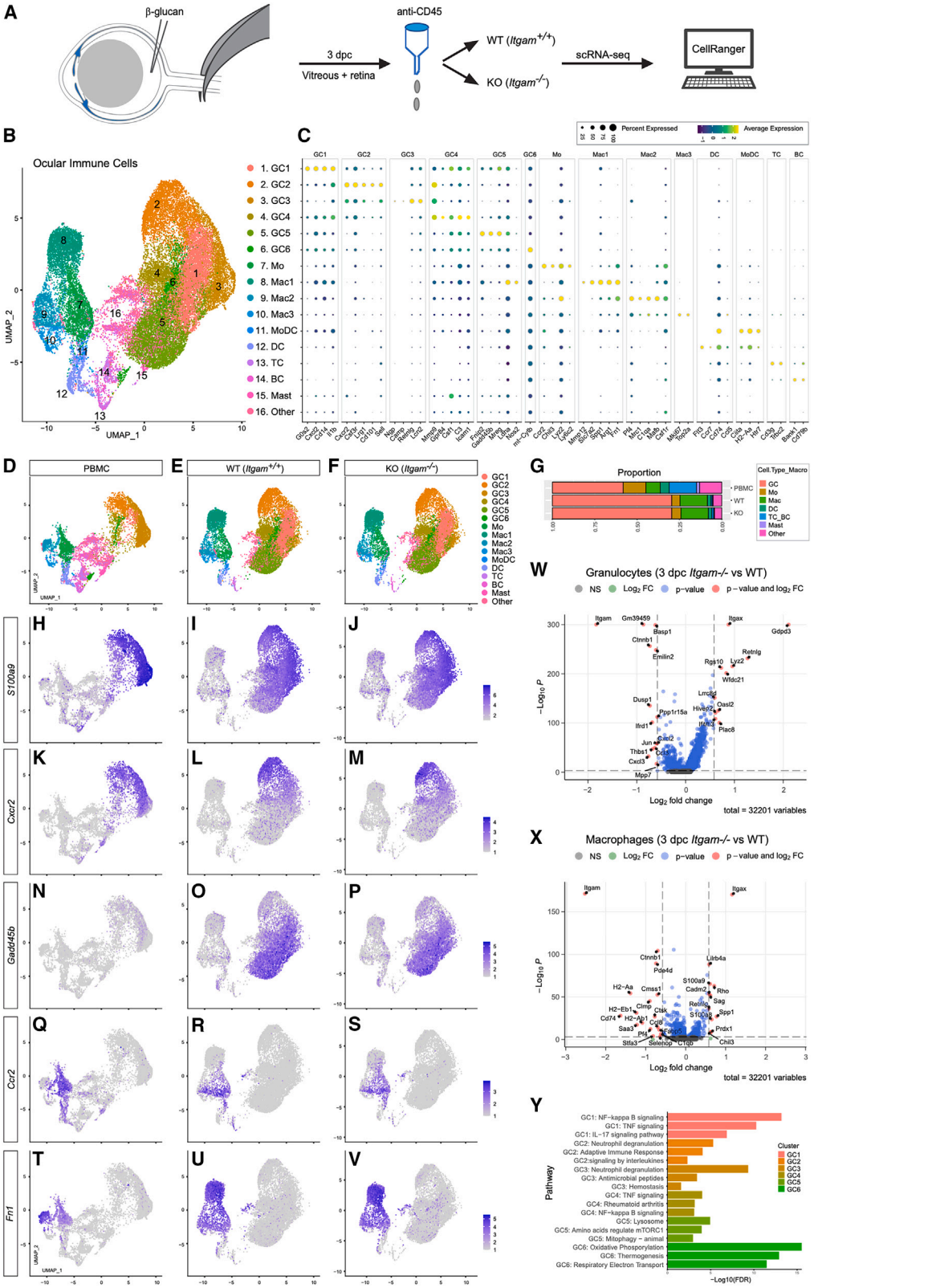

(legend on next page)

(SDF-1/CXCL12), nerve growth factor (*Ngf*), and brain derived growth factor (*Bdnf*) are not identified by scRNA-seq, likely reflecting the limited sequencing depth of this technique.

We identified small clusters representing Mo-derived dendritic cells (moDCs; cluster 11), DCs (cluster 12), T cells (TCs; cluster 13), B cells (cluster 14), and mast cells (cluster 15) (Figures 5C and 5G). While DCs express high levels of *Ccl5*, previously shown to promote RGC regeneration,[58] scRNA-seq did not reveal differences among genotypes (Figures 5D–5V, S6L, and S6M). Compared to GCs in PBMCs, the composition of ocular GCs was more heterogeneous. For example, *Cxcr2*$^{+}$ GCs were found in blood and ocular immune infiltrates, whereas subpopulations of *Tnf*^{hi} and *Gadd45b*^{hi} GCs were only detected in the eye (Figures 5K–5P).

Volcano plots of differentially expressed genes (DEGs), comparing all GCs between WT and *Itgam*$^{-/-}$ eyes, revealed an increase in *Itgax* (CD11c), *Gdpd3* (glycerophosphodiester phosphodiesterase domain-containing 3), *Retnlg* (resistin-like γ), *Lyz2* (lysozyme), and *Rgs10* (regulator of G protein signaling 10) in mutants. As expected, *Itgam* (CD11b) is strongly reduced in mutants, along with *Basp1* (brain abundant membrane attached signal protein 1) and *Ctnnb1* (catenin beta 1) (Figure 5W). Volcano plots comparing all Macs of WT and *Itgam*$^{-/-}$ mice showed a decrease in major histocompatibility complex II molecules and the co-receptor *Cd74* and an increase in *Itgax* (CD11c) in mutants (Figure 5X). Volcano plots of DEGs between WT and *Itgam*$^{-/-}$ Mos, DCs, and TCs are shown (Figures S6N–S6P). In *Itgam*$^{-/-}$ TCs, there is a reduction in CD3 TC receptor subunits (*Cd3g*, *Cd3e*, *Cd3d*) and an increase in the immunoreceptor tyrosine-based inhibitory motif (ITIM)-bearing receptors *Lilr4b* and *Lilrb4a*.

To assign functional specification to GC and Mac subpopulations, the top cluster-enriched gene products were used for pathway analysis with String.db. In both WT and *Itgam*$^{-/-}$ mice, cluster GC1 (enriched for *G0s2*, *Cxcl2*, *Cd14*, *Il1b*, and *Il1a*) represents pro-inflammatory cells, with predicted activation of *nuclear factor κB* (*NF-κB*) *signaling*, *tumor necrosis factor* (*TNF*) *signaling*, and *interleukin-17 signaling* (Figure 5Y). For cluster GC2 (*Cxcr2*, *Csf3r*, *Lrg1*, *Cd101*, *Sell*), pathway analysis revealed *neutrophil degranulation*, *adaptive immune response*, and *signaling by interleukins*. For cluster GC3 (*Ngp*, *Camp*, *Retnlg*, *S100a9*, *Lcn2*), *neutrophil degranulation*, *antimicrobial peptides*, and *S100A9 complex* were revealed. For cluster GC4 (*Mmp9*, *Gpr84*, *Icam1*, *Csf1*), *TNF signaling*, *NF-κB signaling*, and *rheumatoid arthritis* were identified. The elevated expression of *Icam1* in GC4 is suggestive of reverse neutrophil migration.[59] For cluster GC5 (*Fnip2*, *Mreg*, *Ctsb*, *F10*), *lysosome*, *amino acids regulate mTORC1*, and *mitophagy* were identified. Cluster GC6 contains neutrophils enriched for mitochondrial genes, suggesting increased mitochondrial biogenesis or damaged mitochondria in cells that undergo apoptosis (Figure 5Y). Pathway analysis for Mac1 predicts *functions in cell migration* (false discovery rate [FDR]: 2.70e−15), *regulation of cytokine production* (FDR: 7.03e−08), *response to wounding* (FDR: 4.07e−07), *negative regulation of neuron death* (FDR: 1.15e−05), and *response to oxygen levels* (FDR: 1.02e−05) and for Mac 2 predicts *translation/cytosolic ribosome* (FDR: 4.64e−61), *initial triggering of complement* (FDR: 8.36e−06), and *positive regulation of phagocytosis* (FDR: 7.98e−06). Mac3 represents proliferating (*Mki67*$^{+}$) myeloid cells.

Taken together, scRNA-seq analysis identified several subpopulations of conventional neutrophils with pro-inflammatory gene signatures but did not reveal any immature neutrophils. Additionally, inflammation-resolving Mac subpopulations were identified. The reduced ocular inflammation in *Itgam*$^{-/-}$ mice is not attributed to the loss of a specific neutrophil subpopulations but rather to a reduction in leukocyte infiltration.

Analysis of the vitreal proteome of *Itgam*$^{-/-}$ mice reveals protection of the BRB

For an unbiased analysis of the vitreal proteome, we harvested vitreous humor from WT and *Itgam*$^{-/-}$ mice at 3 dpc plus i.o. β-glucan and used label-free mass spectrometry-based proteomics (Figure 6A). For both genotypes, more than 1,400 proteins were identified with high confidence (Table S1). String.db analysis of the 200 most abundant proteins in the WT and *Itgam*$^{-/-}$ vitreous revealed similar functional network enrichments (Figures S7I and S7J). They include *complement and coagulation cascades* (FDRs 1.25e−15 for WT and 7.76e−17 for *Itgam*$^{-/-}$) (Figure 6C), *lens development* (FDRs 2.24e−15 and 3.25e−15, respectively), *glycolysis and gluconeogenesis* (FDRs 2.83e−11 and 2.73e−10, respectively), *fibrinolysis* (FDRs 2.54e−06 and 1.01e−07, respectively), *blood coagulation*, *fibrin clot formation* (FDRs 9.37e−06 and 1.04e−05, respectively), and *blood microparticle* (FDRs 4.65e−06 and 5.19e−06, respectively). The presence of blood microparticles, activation of the coagulation cascade, and fibrin clot formation are strong indicators of retinal vascular damage and ocular microhemorrhage.

Figure 5. The immune response to i.o. β-glucan at single-cell resolution

(A) Workflow of scRNA-seq pipeline.

(B) Uniform manifold approximation and projection (UMAP) embedding of ocular leukocytes together with WT PBMCs. Unsupervised Seurat-based clustering revealed 16 clusters.

(C) Cell types and dot plot analysis of cluster-enriched gene products. Expression levels are normalized to average gene expression, and dot size indicates the percentile of cells expressing the gene.

(D–F) UMAP plots of (D) PBMCs from naive WT mice (E) and UMAP plot of leukocytes in 3 dpc eyes from WT and (F) *Itgam*$^{-/-}$ mice.

(G) Relative cell-type abundance in WT and *Itgam*$^{-/-}$ eyes compared to PBMCs.

(H–V) Feature plots of neutrophil- (*S100a9*, *Cxcr2*, *Gadd45b*), monocyte- (*Ccr2*), and M2-like macrophage- (*Fn1*) associated genes.

(W) Volcano plot of all granulocytes in *Itgam*$^{-/-}$ versus WT eyes.

(X) Volcano plot of all macrophages in *Itgam*$^{-/-}$ versus WT eyes. y axis shows the −log10 p value and the x axis the log2 fold change.

(Y) Pathway analysis of GC subpopulation- (GC1–GC6) enriched gene products shown as −log10 FDR. GC, granulocytes; Mo, monocytes; Mac, macrophages; MoDC, monocyte-derived macrophages; DC, dendritic cells; TC, T cells; BC, B cells; Mast, mast cells; Other, technical artifacts.

See also Figure S6.

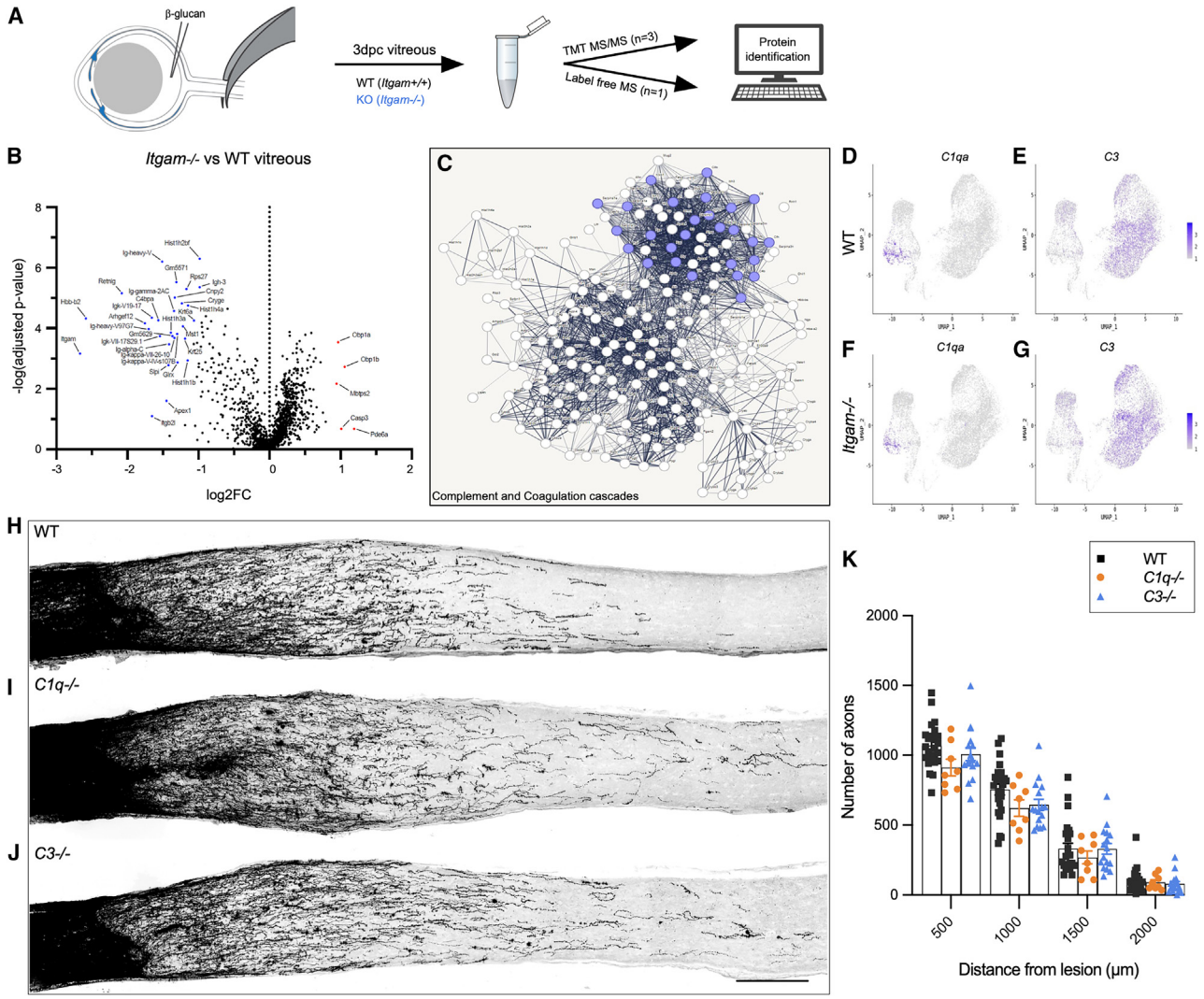

Figure 6. Disruption of the classical complement cascade does not enhance axon regeneration

(A) Schematic of workflow for analysis of vitreous proteome.

(B) Volcano plot of differentially abundant proteins in the *Itgam*$^{-/-}$ versus WT vitreous. y axis is the −log(adjusted) p value and x axis the log2 fold change.

(C) Pathway analysis identifies complement and coagulation cascades (purple).

(D–G) Feature plots of (D and F) *C1q* and (E and G) *C3* expression in ocular immune cells of WT and *Itgam*$^{-/-}$ mice.

(H–J) CTB-traced axons at 14 dpc and i.o. β-glucan of (H) WT (n = 24 nerves), (I) *C1q*$^{-/-}$ (n = 8), and (J) *C3*$^{-/-}$ (n = 8). Scale bar, 200 μm.

(K) Quantification of regenerated axons. Results are presented as mean ± SEM. Data were analyzed with two-way ANOVA followed by Tukey's multiple comparisons. None of the comparisons showed a p value ≤ 0.05.

See also Figure S7 and Tables S1 and S2.

For differential analysis of the WT and *Itgam*$^{-/-}$ vitreal proteome, we used tandem mass tagging and identified 375 proteins with significantly altered abundances (Table S2). When compared to WT vitreous, 159 proteins are decreased and 216 increased in the *Itgam*$^{-/-}$ vitreous (Figure 6B). Strongly downregulated proteins in the *Itgam*$^{-/-}$ vitreous include the integrins CD11b and CD18 (MAC-1). Moreover, hemoglobin b2 and several serum proteins, including immunoglobulin chains, β2-glycoprotein 1, albumin, fibrinogen, and afamin, were reduced in the *Itgam*$^{-/-}$ vitreous, suggestive of reduced vascular damage. Furthermore, there is a reduction in neutrophil extracellular trap (NET)-associated proteins, including histone subunits (H1, H2, H3, H4), cathepsin G, myeloperoxidase (MPO), matrix metalloproteinase-9 (MMP9), neutrophilic granule protein/*Ngp*, and neutrophil elastase/*Elane*. String.db analysis of proteins reduced in the *Itgam*$^{-/-}$ versus WT vitreous identified *complement and coagulation cascades* (FDR 3.68e−12), *complement activation, classical pathway* (FDR 4.73e−05), *leukocyte migration* (FDR 3.03e−07), *NETosis of peripheral neutrophils* (FDR 1.05e−05), and *activation of matrix metalloproteases* (FDR 1.75e−05). String.db analysis of proteins elevated in the *Itgam*$^{-/-}$ versus WT vitreous identified *translation* (FDR 1.56e−09), *hemostasis*

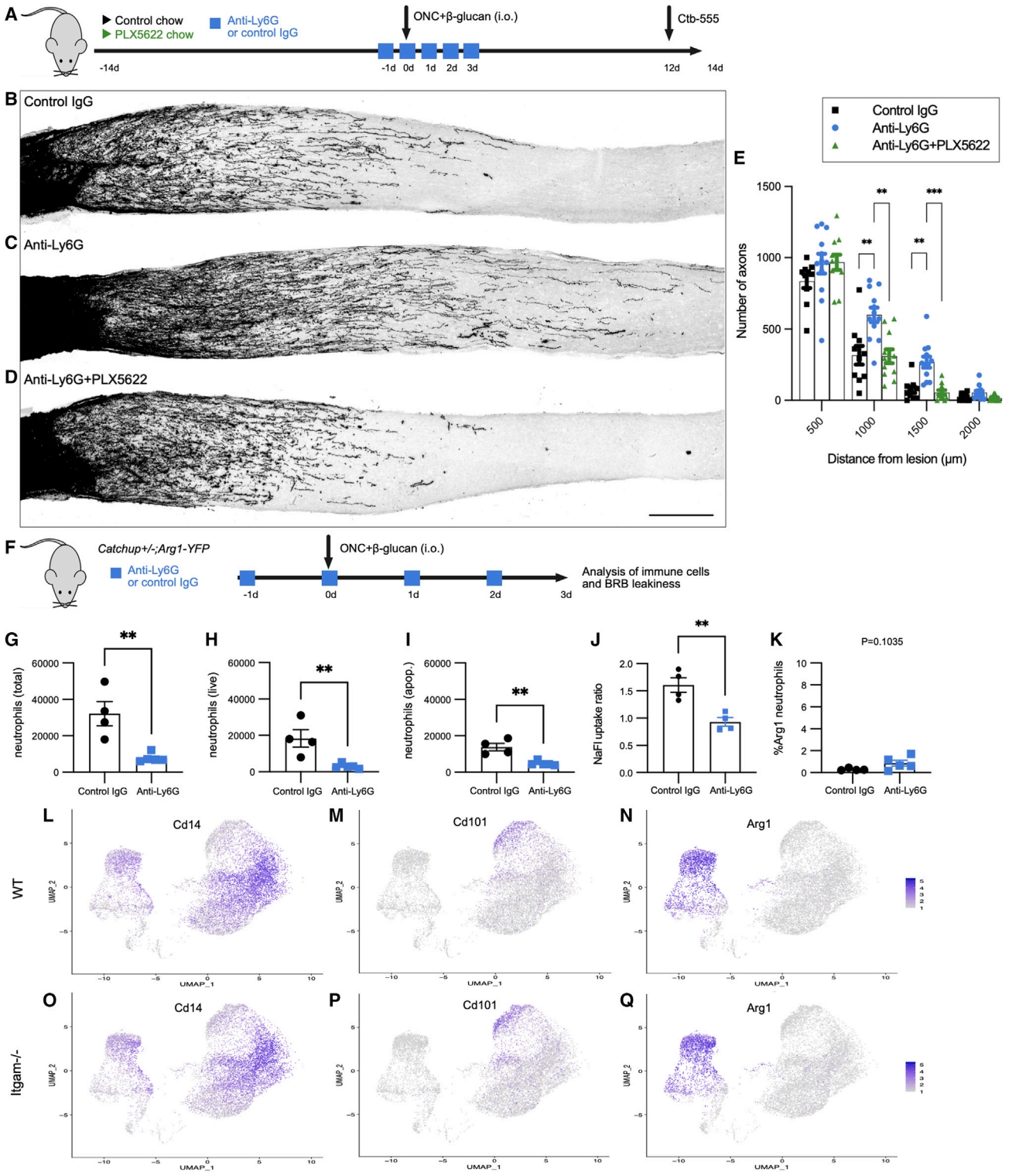

Figure 7. In β-glucan-treated mice, anti-Ly6G results in enhanced RGC axon regeneration

(A) Experimental timeline of anti-Ly6G treatment.

(B–D) CTB-traced axons at 14 dpc plus i.o. β-glucan in mice treated with (B) control IgG, (C) anti-Ly6G, and (D) anti-Ly6G on PLX5622 chow. Scale bar, 200 μm.

(E) Quantification of regenerated axons. Control IgG (n = 10 nerves); anti-Ly6G (n = 11); anti-Ly6G on PLX5622 (n = 12). Results are presented as mean ± SEM. Data were analyzed with two-way ANOVA followed by Tukey's multiple comparisons. **p ≤ 0.01 and ***p ≤ 0.001.

(legend continued on next page)

and acute phase (FDR 2.72e−10), *glycolysis and gluconeogenesis* (FDR 4.48e−09), and *high-density lipoprotein particle* (FDR 3.73e−05). The reduction in neutrophil-associated proteins in the *Itgam*$^{-/-}$ vitreous is consistent with flow cytometric studies where fewer neutrophils were detected in *Itgam*$^{-/-}$ eyes (Figure 4). Differences in classical complement pathway were of interest because *Itgam* encodes CD11b, a vital component of the complement receptor CR3.

Enhanced RGC regeneration in *Itgam*$^{-/-}$ mice is not due to disruption of the classical complement cascade

Complement has been shown to function in nervous system development, degeneration, and regeneration.[39,60–62] Consistent with proteomics studies, complement *C1q* and *C3* transcripts are upregulated by ocular immune cells, as assessed by scRNA-seq (Figures 6C–6G). We therefore wondered whether the enhanced RGC regeneration observed in *Itgam*$^{-/-}$ mice is due to impairment of the classical complement cascade. To test this idea, mice deficient for C1q (*C1q*$^{-/-}$), the initiating protein of the classical complement cascade, or the downstream complement protein C3 (*C3*$^{-/-}$) were subjected to ONC and i.o. β-glucan injection. After 2 weeks, regenerated axons in optic nerve sections were compared to parallel-processed WT mice (Figures 6H–6J). Quantification of axon length and number revealed very similar regeneration among all three genotypes (Figure 6K). This shows that enhanced RGC axon regeneration observed in *Itgam*$^{-/-}$ mice is not due to disruption of the classical complement cascade.

In β-glucan-treated mice, anti-Ly6G protects the BRB and enhances RGC axon regeneration

Because *Itgam* is broadly expressed by innate immune cells, we next treated mice with the monoclonal antibody 1A8, directed against the neutrophil-specific surface protein Ly6G. Anti-Ly6G and isotype control IgG were administered systemically 1 day before ONC and i.o. β-glucan, with additional doses at the time of ONC and after injury. At 14 dpc, optic nerves were harvested and regenerated axons quantified (Figure 7A). Mice treated with anti-Ly6G, but not control IgG, showed significantly enhanced RGC axon regeneration (Figures 7B–7E). This suggests that antibody-mediated depletion of neutrophils is sufficient to enhance β-glucan-elicited optic nerve axon regeneration. To assess the efficacy of neutrophil depletion, we treated *Catchup*$^{+/-}$ mice with anti-Ly6G or control IgG (Figure 7F). Flow cytometry of ocular inflammation at 3 dpc plus i.o. β-glucan revealed that the total number of neutrophils (tdT^{+} cells), live neutrophils (Tdt^{+}, nuclear viability stain^{-}), and apoptotic neutrophils (tdT^{+}, annexin A5/AnxaV^{+}) were reduced in anti-Ly6G-treated mice (Figures 7G–7I). Thus, anti-Ly6G results in a significant, yet incomplete, reduction in neutrophil transmigration. Because excessive neutrophil transmigration has been associated with vascular damage,[63,64] increased RGC regeneration in anti-Ly6G may be a result of improved vascular integrity. Indeed, anti-Ly6G protected the inflamed retinal vasculature and reduced BRB leakiness (Figure 7J).

Because microglia have been shown to protect the neurovasculature and to phagocytose extravasated neutrophils,[19,65] we wondered whether the pro-regenerative effects of anti-Ly6G are sensitive to microglia ablation. RGC regeneration studies with PLX5622-fed mice revealed that the pro-regenerative effects of anti-Ly6G are no longer observed (Figures 7D and 7E). Thus, microglia are necessary for the beneficial effects of anti-Ly6G, underscoring the opposing effects of neutrophils and microglia on injured neurons.

Anti-Ly6G does not skew eye-infiltrating neutrophils toward an Arg1^{+} phenotype

To examine whether systemic anti-Ly6G skews neutrophils toward an immature Arg1^{+} phenotype that supports RGC regeneration, as demonstrated for anti-CXCR2 treatment,[29] we crossed *Catchup*$^{+/-}$ mice with *Arg1-YFP*$^{+/-}$ mice to generate a double-reporter line. At 3 dpc and i.o. β-glucan, we analyzed vitreous and retinas of anti-Ly6G- and control-IgG-treated reporter mice using flow cytometry (Figure S4T). Control-IgG-treated mice showed only a small number of Arg1^{+} neutrophils (<1%), and there was no increase observed in anti-Ly6G-treated mice (Figure 7K). Commensurate with this finding, scRNA-seq analysis of ocular immune filtrates did not find an increase in *Cd14*$^{+}$ neutrophils or decrease in *Cd101*$^{+}$ neutrophils (Figures 7L, 7M, 7O, and 7P). Although a subpopulation of *Arg1*^{hi} cells (cluster 8) was identified in WT and *Itgam*$^{-/-}$ mice by scRNA-seq, these are Macs, and they show little change upon *Itgam* ablation (Figures 7N and 7Q).

DISCUSSION

We provide multiple lines of evidence showing that protecting vascular integrity in the murine retina enhances immune-mediated RGC axon regeneration. Through the depletion of select immune cell populations, we have shown that microglia play a beneficial role and contribute to the success of RGC regeneration, whereas pro-inflammatory (conventional) neutrophils have a detrimental impact. Under normal circumstances, i.o. β-glucan induces rapid accumulation of neutrophils in the retinal vasculature, where they undergo massive transmigration out of postcapillary venules, entering the retinal parenchyma and vitreous. Functional ablation of CD11b attenuates β-glucan-elicited ocular inflammation, protects the BRB, and enhances RGC axon regeneration, and this is not due to disruption of the classical

(F) Experimental timeline for flow cytometry and assessment of vascular integrity.
(G–I) Quantification of (G) total neutrophils, (H) live neutrophils, and (I) apoptotic neutrophils from eyes of *Catchup*$^{+/-}$ mice.
(J) Quantification of BRB leakiness at 3 dpc plus i.o. β-glucan with systemic control IgG (n = 4) and anti-Ly6G (n = 4). Data were analyzed using unpaired Student's t test. **p ≤ 0.01.
(K) Percentage of tdT^{+} ocular neutrophils that are Arg1^{+} at 3 dpc plus i.o. β-glucan. Flow data are presented as mean ± SEM. Statistical analysis, unpaired Student's t test. **p ≤ 0.01.
(L–Q) Feature plots of *Cd14*, *Cd101*, and *Arg1* expression in WT (L–N) and *Itgam*$^{-/-}$ (O–Q) ocular immune infiltrates. Color-coded calibration of log2-fold gene expression is shown.

complement cascade. Transcriptomic studies identified subpopulations of classically activated neutrophils in the eye. Selective targeting of neutrophils with systemic anti-Ly6G resulted in a notable reduction of retinal neutrophils, decreased BRB permeability, and enhanced RGC regeneration, highlighting the detrimental effects of neutrophils on neurorepair. The observed beneficial effects in *Itgam*$^{-/-}$ mice and anti-Ly6G-treated mice are not attributable to an increase in alternatively activated Arg1^{+} neutrophils but rather to a decrease in pro-inflammatory neutrophils. Based on these findings, we propose that protecting the inflamed vasculature represents a target for promoting neuronal regeneration. Therapeutic strategies aimed at preserving microvascular integrity and neurovascular coupling may hold promise for CNS repair.

Code for unbiased quantification of regenerated axons

Building on previous observations,[30] we found that particulate, but not soluble, forms of β-glucan promote RGC regeneration. While the regenerative effects of particulate β-glucan are more robust compared to zymosan, reliable quantification of regenerated RGC axons in optic nerve sections remains technically challenging. To address this problem, we developed software that enables unbiased identification and quantification of CTB-traced axons in nerve images at any distance from the crush site. By writing code specifically for this purpose, our hope is to help standardizing the quantification of regenerated axons and thereby facilitate comparisons among different studies and experimental treatments.

Neutrophil-inflicted vascular damage limits CNS neuron regeneration

The importance of neutrophils in immune-mediated RGC axon regeneration was established more than a decade ago.[31] Subsequent studies revealed neutrophil heterogeneity and led to the identification of unconventional neutrophils with axogenic properties.[29] Although neutrophil heterogeneity has also been observed in tumors and infected and injured tissues, the attribution of subset-specific functions remains challenging.[66] Using scRNA-seq, we show that conventional neutrophils respond to i.o. β-glucan and readily accumulate in the vitreous. We identified six different neutrophil subsets (GC1–GC6) that are pro-inflammatory in nature. Pathway analysis infers release of chemokines, proteases, degranulation, and NET formation. The overabundance of pro-inflammatory neutrophils that respond to i.o. β-glucan likely contributes to collateral tissue damage.[67]

Conversely, we show that microglia are beneficial for immune-mediated RGC regeneration. In addition to shielding the microvasculature from endothelial damage, microglia rapidly phagocytose extravascular neutrophils.[19,65] While conventional neutrophils play critical roles in the host defense response, including NET-mediated entrapment of pathogens and containment of infections, prolonged neutrophil activation has detrimental effects. Classically activated neutrophils release reactive oxygen species that damage the endothelium, and NETs are known to promote coagulation and cause microthrombi. NET-associated histones and MPO induce endothelial cell death, and proteases associated with NETs can disrupt the junctional adhesion complexes among endothelial cells, causing breakdown of the BRB and the blood-brain barrier.[68–72] Moreover, neutrophilic proteases detected in the vitreous upon i.o. β-glucan, including extracellular cathepsin G, NE, MPO, and MMP9, exert strong toxic effects toward neurons.[73] Thus, microglia may not only protect the BRB from neutrophil-inflicted damage but also phagocytose extravascular neutrophils, thereby mitigating toxic effects toward RGCs.

Our findings may have far-reaching implications beyond β-glucan-elicited neurorepair. The interaction between classically activated neutrophils and the vascular endothelium is emerging as a key orchestrator of neural repair.[74] In stroke models, protecting the neurovasculature from neutrophil-induced damage has been shown to reduce infarct volume and improve neurological outcomes.[75] In Alzheimer's disease (AD) models, neutrophils have been observed to selectively migrate near regions with amyloid-β deposits where they release NETs, and importantly, temporary depletion of neutrophils attenuates early stages of cognitive decline.[76] Moreover, administration of anti-Ly6G increases cerebral blood flow in AD models.[70,71] When considering these findings alongside our studies in the injured visual system, our results suggest that safeguarding the inflamed microvasculature within the injured CNS is beneficial for neural repair following trauma, stroke, and neurodegenerative disorders.

Arg1^{+} Macs are an abundant source of pro-regenerative factors

Upon microglia depletion, β-glucan-elicited RGC regeneration is reduced, though axon regeneration remains significantly elevated compared to control mice not injected with β-glucan. This points to microglia-independent mechanisms associated with immune-mediated neurorepair. Although the pro-regenerative immune cells were not the focus of the current study, we identified resolving (healing) Macs that accumulate in the vitreous upon i.o. β-glucan in both WT and *Itgam*$^{-/-}$ mice. A subpopulation of *Arg1*^{hi} Macs expresses numerous molecular players known to promote RGC protection and axon regeneration. We speculate that the protection of the inflamed vasculature from neutrophil-induced damage enhances the RGC-regenerative response triggered by *Arg1*^{hi} Macs. Shielding the microvasculature from neutrophil-inflicted damage aids oxygen and nutrient supply to injured RGCs and, in addition, reduces retinal accumulation of neutrophil-derived growth-inhibitory proteases.[73] Consistent with this idea, ELISA of retinal lysates revealed a reduction in neutrophil-associated proteins in *Itgam*$^{-/-}$ mice. Moreover, the vitreal proteome of *Itgam*$^{-/-}$ mice showed a reduction in serum proteins and NET-associated proteins.

Functional ablation of CD11b protects the inflamed vasculature and promotes RGC regeneration independently of the classical complement cascade

The integrin CD11b is a pleotropic molecule found on the surface of nearly all innate immune cells and, depending on the context, exerts many different functions. The αM-I domain of CD11b is located near the N terminus and comprises the main ligand binding site, accommodating numerous ligands.[54] While best known for its function as a vital component of the complement receptor 3 (MAC-1), we find that loss of *C1q* or *C3* does not mimic the enhanced RGC regeneration observed in *Itgam*$^{-/-}$ mice.

Although this observation seems at variance with a recent study,[61] important technical differences were noted, including the use of zymosan combined with cAMP by Peterson et al. rather than purified β-glucan without cAMP that was used in the current study.

In the brain, extravascular fibrinogen binds to CD11b on perivascular microglia and contributes to axonal damage in neuroinflammatory disease.[77] Although disrupting this interaction may contribute to the beneficial effects observed in *Itgam*$^{-/-}$ mice, the diminished regeneration following microglia depletion suggests the involvement of other mechanisms, ultimately shifting the overall function of microglia toward a net positive outcome. Moreover, MAC-1 interacts with MPO, triggering a further increase in MPO release, creating a feedforward loop that amplifies the inflammatory response. The transfer of MPO from neutrophils to endothelial cells contributes to vasculitis and the disruption of normal endothelial cell function.[78,79] Since MPO levels are reduced in the vitreous of *Itgam*$^{-/-}$ mice, this reduction may ultimately contribute to improved vascular health.

Noteworthy, CD11b has a lectin domain, distinct from the αM-I domain, that directly binds β-glucan and participates in phagocytosis of zymosan and β-glucan and the production of reactive oxygen species (ROS).[80] Particulate β-glucan is too large to be cleared by phagocytosis and, in the presence of fibronectin, suppresses ROS production. Instead, particulate β-glucan and fibronectin induce NET formation to combat fungal infection,[54,81] and as discussed above, NETs can cause vascular damage. While β-glucan is known to bind to several surface receptors, including CD11b, the main immune mechanisms underlying enhanced RGC regeneration involve dectin-1 and Toll-like receptor 2.[30] Additional studies with CD11b mutants, selectively deficient for lectin activity, will be needed to determine the functional significance of the CD11b interaction with β-glucan.

Anti-Ly6G does not result in the occurrence of Arg1^{+} axogenic neutrophils

Although our studies point to a detrimental effect of conventional neutrophils, they do not fully rule out the occurrence of axogenic neutrophils[29] since anti-Ly6G and functional ablation of CD11b only partially block neutrophil trafficking into the eye upon i.o. β-glucan. However, unlike anti-CXCR2 treatment, scRNA-seq revealed that *Itgam* deficiency does not result in a shift away from *Cd101*^{hi} conventional neutrophils or an increase in immature *Cd14*^{hi} neutrophils.[29] In a similar vein, anti-Ly6G does not push neutrophils toward an Arg1^{+} phenotype but rather reduces trafficking of neutrophils into the eye. Collectively, these findings indicate that the mechanistic underpinnings of enhanced RGC regeneration described here are distinct from the ones following anti-CXCR2 treatment combined with i.o. zymosan.[29] Commensurate with this conclusion, analysis of PBMCs revealed that Ly6G^{hi} and CXCR2^{hi} neutrophils mark different subsets: immature and mature neutrophils, respectively.[55,69] Here we propose that a reduction in conventional neutrophils is beneficial because it protects the retinal vasculature and BRB, facilitating effective transport of nutrients and oxygen supply to injured RGCs.

Limitations of the study

We demonstrate that in the context of immune-mediated RGC regeneration, microglia exhibit beneficial effects, while conventional neutrophils have detrimental effects, attributed to their opposing impacts on vascular integrity. However, there are certain limitations to our study. For instance, to establish a causal link between RGC regeneration and the BRB, it will be necessary to directly manipulate BRB integrity independently of immune cell manipulations. *In vivo*, depletion of specific immune cell populations is very challenging. Although significant depletion of microglia and reduction of neutrophil migration into the eye were achieved in the current study, none of the manipulations were complete. This leaves open the formal possibility that some of the remaining ∼10% microglia exert detrimental effects toward RGCs. Conversely, it is possible that some of the remaining neutrophils entering the eye following CD11b or Ly6G ablation promote RGC regeneration.

Myeloid cell heterogeneity is well established and increases upon injury; however, subpopulation-specific functions remain incompletely understood. Our multiomics studies identified several subpopulations of classically activated neutrophils massively accumulating in the eye, contributing to elevated levels of MPO, histones, and proteases associated with NETs in the vitreous. While neutrophils and NET proteins were reduced in *Itgam*$^{-/-}$ mice, the precise mechanisms by which neutrophils inflict vascular damage and BRB leakiness and ultimately inhibit RGC regeneration remain incompletely understood. Finally, scRNA-seq studies of ocular leukocytes and the analysis of vitreal proteomes were conducted at only one post-injury time point and were limited to two biological replicates and three technical replicates, respectively.

STAR★METHODS

Detailed methods are provided in the online version of this paper and include the following:

- KEY RESOURCES TABLE
- RESOURCE AVAILABILITY
  - Lead contact
  - Materials availability
  - Data and code availability
- EXPERIMENTAL MODEL AND STUDY PARTICIPANT DETAILS
  - Mice
- METHOD DETAILS
  - Microglia ablation
  - Optic nerve surgery and intra-ocular injections
  - Antibody treatment
  - Flow cytometry
  - Optic nerve analysis
  - Retinal analysis
  - Assessment of BRB integrity
  - Multiplex ELISA
  - scRNA-sequencing
  - scRNAseq data analysis
  - Proteomics of vitreous
  - High pH reverse phase chromatography

SUPPLEMENTAL INFORMATION

Supplemental information can be found online at https://doi.org/10.1016/j.celrep.2024.113931.

ACKNOWLEDGMENTS

We thank members of the Giger laboratory for critical reading of the manuscript, David Antonetti and Chengmao Lin for help with assessing BRB leakiness, Olivia Nelson for help with RGC survival experiments, and Qing Wang for excellent technical support. This work was supported by the National Institutes of Health, Ruth Kirschstein Fellowships 1F31NS135919-01 (H.H.) and MH119346 (R.J.G.), the University of Michigan MICHR seed funds (R.J.G.), and the Dr. Miriam and Sheldon G. Adelson Medical Research Foundation (A.L.B., D.H.G., L.I.B., and R.J.G.). We thank Dr. Richard Locksley for *Arg1-YFP* and Dr. Ki-Wook Kim for *Catchup* reporter mice.

AUTHOR CONTRIBUTIONS

Conceptualization, R.P. and R.J.G.; methodology, R.P., M.C.F., H.H., Q.F., L.D.H., X.-F.Z., C.J., R.K., and J.A.O.-P.; software, M.C.F. and C.J.; formal analysis, R.P., M.C.F., H.H., Q.F., L.D.H., X.-F.Z., C.J., and J.A.O.-P.; data curation, C.J. and J.A.O.-P.; visualization, R.P., C.J., H.H., L.D.H., and Q.F.; writing – original draft, R.J.G.; writing – review & editing, R.P., H.H., L.I.B., and R.J.G.; funding acquisition, A.L.B., D.H.G., L.I.B., and R.J.G.; resources, A.L.B., D.H.G., and R.J.G.; supervision, A.L.B., D.H.G., and R.J.G.

DECLARATION OF INTERESTS

Particulate and soluble β-(1,3)(1,6)-glucans were provided by ImmunoResearch, Inc., MN 55121, USA, under a collaborative research agreement. The PLX5622 compound was provided by Plexxikon, Inc., San Francisco, California, USA. Neither ImmunoResearch, Inc., nor Plexxikon, Inc., had any input in experimental design, data acquisition, interpretation, or presentation.

Received: September 24, 2023
Revised: January 3, 2024
Accepted: February 21, 2024
Published: March 15, 2024

REFERENCES

1. Benowitz, L.I., Xie, L., and Yin, Y. (2023). Inflammatory Mediators of Axon Regeneration in the Central and Peripheral Nervous Systems. Int. J. Mol. Sci. *24*, 15359. https://doi.org/10.3390/ijms242015359.
2. Todorov, V., and Dimitrova, M. (2020). Stroke and the immune system: A review of the new strategies. Folia Med. *62*, 431–437. https://doi.org/10.3897/folmed.62.e49451.
3. Tsygan, N.V., Trashkov, A.P., Litvinenko, I.V., Yakovleva, V.A., Ryabtsev, A.V., Vasiliev, A.G., and Churilov, L.P. (2019). Autoimmunity in acute ischemic stroke and the role of blood-brain barrier: the dark side or the light one. Front. Med. *13*, 420–426. https://doi.org/10.1007/s11684-019-0688-6.
4. Katsumoto, A., Takeuchi, H., Takahashi, K., and Tanaka, F. (2018). Microglia in Alzheimer's Disease: Risk Factors and Inflammation. Front. Neurol. *9*, 978. https://doi.org/10.3389/fneur.2018.00978.
5. Brennan, F.H., and Popovich, P.G. (2018). Emerging targets for reprograming the immune response to promote repair and recovery of function after spinal cord injury. Curr. Opin. Neurol. *31*, 334–344. https://doi.org/10.1097/WCO.0000000000000550.
6. Busch, S.A., Horn, K.P., Silver, D.J., and Silver, J. (2009). Overcoming macrophage-mediated axonal dieback following CNS injury. J. Neurosci. *29*, 9967–9976. https://doi.org/10.1523/JNEUROSCI.1151-09.2009.
7. Brennan, F.H., Jogia, T., Gillespie, E.R., Blomster, L.V., Li, X.X., Nowlan, B., Williams, G.M., Jacobson, E., Osborne, G.W., Meunier, F.A., et al. (2019). Complement receptor C3aR1 controls neutrophil mobilization following spinal cord injury through physiological antagonism of CXCR2. JCI Insight *4*, e98254. https://doi.org/10.1172/jci.insight.98254.
8. Cai, X.F., Lin, S., Geng, Z., Luo, L.L., Liu, Y.J., Zhang, Z., Liu, W.Y., Chen, X., Li, X., Yan, J., and Ye, J. (2020). Integrin CD11b Deficiency Aggravates Retinal Microglial Activation and RGCs Degeneration After Acute Optic Nerve Injury. Neurochem. Res. *45*, 1072–1085. https://doi.org/10.1007/s11064-020-02984-6.
9. Liddelow, S.A., Guttenplan, K.A., Clarke, L.E., Bennett, F.C., Bohlen, C.J., Schirmer, L., Bennett, M.L., Münch, A.E., Chung, W.S., Peterson, T.C., et al. (2017). Neurotoxic reactive astrocytes are induced by activated microglia. Nature *541*, 481–487. https://doi.org/10.1038/nature21029.
10. Mou, Q., Yao, K., Ye, M., Zhao, B., Hu, Y., Lou, X., Li, H., Zhang, H., and Zhao, Y. (2021). Modulation of Sirt1-mTORC1 Pathway in Microglia Attenuates Retinal Ganglion Cell Loss After Optic Nerve Injury. J. Inflamm. Res. *14*, 6857–6869. https://doi.org/10.2147/JIR.S338815.
11. Hilla, A.M., Diekmann, H., and Fischer, D. (2017). Microglia Are Irrelevant for Neuronal Degeneration and Axon Regeneration after Acute Injury. J. Neurosci. *37*, 6113–6124. https://doi.org/10.1523/JNEUROSCI.0584-17.2017.
12. Feng, Q., Wong, K.A., and Benowitz, L.I. (2023). Full-length optic nerve regeneration in the absence of genetic manipulations. JCI Insight *8*, e164579. https://doi.org/10.1172/jci.insight.164579.
13. Siddiqui, A.M., Sabljic, T.F., and Ball, A.K. (2022). Anatomical location of injected microglia in different activation states and time course of injury determines survival of retinal ganglion cells after optic nerve crush. Int. J. Neurosci., 1–23. https://doi.org/10.1080/00207454.2022.2142579.
14. Marino Lee, S., Hudobenko, J., McCullough, L.D., and Chauhan, A. (2021). Microglia depletion increase brain injury after acute ischemic stroke in aged mice. Exp. Neurol. *336*, 113530. https://doi.org/10.1016/j.expneurol.2020.113530.
15. Hamner, M.A., McDonough, A., Gong, D.C., Todd, L.J., Rojas, G., Hodecker, S., Ransom, C.B., Reh, T.A., Ransom, B.R., and Weinstein, J.R. (2022). Microglial depletion abolishes ischemic preconditioning in white matter. Glia *70*, 661–674. https://doi.org/10.1002/glia.24132.
16. Bellver-Landete, V., Bretheau, F., Mailhot, B., Vallières, N., Lessard, M., Janelle, M.E., Vernoux, N., Tremblay, M.È., Fuehrmann, T., Shoichet, M.S., and Lacroix, S. (2019). Microglia are an essential component of the neuroprotective scar that forms after spinal cord injury. Nat. Commun. *10*, 518. https://doi.org/10.1038/s41467-019-08446-0.
17. Fu, H., Zhao, Y., Hu, D., Wang, S., Yu, T., and Zhang, L. (2020). Depletion of microglia exacerbates injury and impairs function recovery after spinal cord injury in mice. Cell Death Dis. *11*, 528. https://doi.org/10.1038/s41419-020-2733-4.
18. Willis, E.F., MacDonald, K.P.A., Nguyen, Q.H., Garrido, A.L., Gillespie, E.R., Harley, S.B.R., Bartlett, P.F., Schroder, W.A., Yates, A.G., Anthony, D.C., et al. (2020). Repopulating Microglia Promote Brain Repair in an IL-6-Dependent Manner. Cell *180*, 833–846.e16. https://doi.org/10.1016/j.cell.2020.02.013.
19. Neumann, J., Sauerzweig, S., Rönicke, R., Gunzer, F., Dinkel, K., Ullrich, O., Gunzer, M., and Reymann, K.G. (2008). Microglia cells protect neurons by direct engulfment of invading neutrophil granulocytes: a new mechanism of CNS immune privilege. J. Neurosci. *28*, 5965–5975. https://doi.org/10.1523/JNEUROSCI.0060-08.2008.
20. Werneburg, S., Feinberg, P.A., Johnson, K.M., and Schafer, D.P. (2017). A microglia-cytokine axis to modulate synaptic connectivity and function. Curr. Opin. Neurobiol. *47*, 138–145. https://doi.org/10.1016/j.conb.2017.10.002.

21. Lou, N., Takano, T., Pei, Y., Xavier, A.L., Goldman, S.A., and Nedergaard, M. (2016). Purinergic receptor P2RY12-dependent microglial closure of the injured blood-brain barrier. Proc. Natl. Acad. Sci. USA *113*, 1074–1079. https://doi.org/10.1073/pnas.1520398113.

22. Mondo, E., Becker, S.C., Kautzman, A.G., Schifferer, M., Baer, C.E., Chen, J., Huang, E.J., Simons, M., and Schafer, D.P. (2020). A Developmental Analysis of Juxtavascular Microglia Dynamics and Interactions with the Vasculature. J. Neurosci. *40*, 6503–6521. https://doi.org/10.1523/JNEUROSCI.3006-19.2020.

23. Zarb, Y., Sridhar, S., Nassiri, S., Utz, S.G., Schaffenrath, J., Maheshwari, U., Rushing, E.J., Nilsson, K.P.R., Delorenzi, M., Colonna, M., et al. (2021). Microglia control small vessel calcification via TREM2. Sci. Adv. *7*, eabc4898. https://doi.org/10.1126/sciadv.abc4898.

24. Barkaway, A., Attwell, D., and Korte, N. (2022). Immune-vascular mural cell interactions: consequences for immune cell trafficking, cerebral blood flow, and the blood-brain barrier. Neurophotonics *9*, 031914. https://doi.org/10.1117/1.NPh.9.3.031914.

25. Haruwaka, K., Ikegami, A., Tachibana, Y., Ohno, N., Konishi, H., Hashimoto, A., Matsumoto, M., Kato, D., Ono, R., Kiyama, H., et al. (2019). Dual microglia effects on blood brain barrier permeability induced by systemic inflammation. Nat. Commun. *10*, 5816. https://doi.org/10.1038/s41467-019-13812-z.

26. Bisht, K., Okojie, K.A., Sharma, K., and Lentferink, D.H. (2021). Capillary-associated microglia regulate vascular structure and function through PANX1-P2RY12 coupling in mice. Nature *12*, 5289. https://www.nature.com/articles/s41467-021-25590-8.

27. Williams, P.R., Benowitz, L.I., Goldberg, J.L., and He, Z. (2020). Axon Regeneration in the Mammalian Optic Nerve. Annu. Rev. Vis. Sci. *6*, 195–213. https://doi.org/10.1146/annurev-vision-022720-094953.

28. Yin, Y., Cui, Q., Li, Y., Irwin, N., Fischer, D., Harvey, A.R., and Benowitz, L.I. (2003). Macrophage-derived factors stimulate optic nerve regeneration. J. Neurosci. *23*, 2284–2293. https://doi.org/10.1523/JNEUROSCI.23-06-02284.2003.

29. Sas, A.R., Carbajal, K.S., Jerome, A.D., Menon, R., Yoon, C., Kalinski, A.L., Giger, R.J., and Segal, B.M. (2020). A new neutrophil subset promotes CNS neuron survival and axon regeneration. Nat. Immunol. *21*, 1496–1505. https://doi.org/10.1038/s41590-020-00813-0.

30. Baldwin, K.T., Carbajal, K.S., Segal, B.M., and Giger, R.J. (2015). Neuroinflammation triggered by β-glucan/dectin-1 signaling enables CNS axon regeneration. Proc. Natl. Acad. Sci. USA *112*, 2581–2586. https://doi.org/10.1073/pnas.1423221112.

31. Kurimoto, T., Yin, Y., Habboub, G., Gilbert, H.Y., Li, Y., Nakao, S., Hafezi-Moghadam, A., and Benowitz, L.I. (2013). Neutrophils express oncomodulin and promote optic nerve regeneration. J. Neurosci. *33*, 14816–14824. https://doi.org/10.1523/JNEUROSCI.5511-12.2013.

32. Wong, K.A., and Benowitz, L.I. (2022). Retinal Ganglion Cell Survival and Axon Regeneration after Optic Nerve Injury: Role of Inflammation and Other Factors. Int. J. Mol. Sci. *23*, 10179. https://doi.org/10.3390/ijms231710179.

33. Xie, L., Cen, L.P., Li, Y., Gilbert, H.Y., Strelko, O., Berlinicke, C., Stavarache, M.A., Ma, M., Wang, Y., Cui, Q., et al. (2022). Monocyte-derived SDF1 supports optic nerve regeneration and alters retinal ganglion cells' response to Pten deletion. Proc. Natl. Acad. Sci. USA *119*, e2113751119. https://doi.org/10.1073/pnas.2113751119.

34. Xie, L., Yin, Y., Jayakar, S., Kawaguchi, R., Wang, Q., Peterson, S., Shi, C., Turnes, B.L., Zhang, Z., Oses-Prieto, J., et al. (2023). The oncomodulin receptor ArmC10 enables axon regeneration in mice after nerve injury and neurite outgrowth in human iPSC-derived sensory neurons. Sci. Transl. Med. *15*, eadg6241. https://doi.org/10.1126/scitranslmed.adg6241.

35. Leibinger, M., Müller, A., Andreadaki, A., Hauk, T.G., Kirsch, M., and Fischer, D. (2009). Neuroprotective and axon growth-promoting effects following inflammatory stimulation on mature retinal ganglion cells in mice depend on ciliary neurotrophic factor and leukemia inhibitory factor. J. Neurosci. *29*, 14334–14341. https://doi.org/10.1523/JNEUROSCI.2770-09.2009.

36. Gensel, J.C., Nakamura, S., Guan, Z., van Rooijen, N., Ankeny, D.P., and Popovich, P.G. (2009). Macrophages promote axon regeneration with concurrent neurotoxicity. J. Neurosci. *29*, 3956–3968. https://doi.org/10.1523/JNEUROSCI.3992-08.2009.

37. Qi, C., Cai, Y., Gunn, L., Ding, C., Li, B., Kloecker, G., Qian, K., Vasilakos, J., Saijo, S., Iwakura, Y., et al. (2011). Differential pathways regulating innate and adaptive antitumor immune responses by particulate and soluble yeast-derived β-glucans. Blood *117*, 6825–6836. https://doi.org/10.1182/blood-2011-02-339812.

38. Tan, Z., Guo, Y., Shrestha, M., Sun, D., Gregory-Ksander, M., and Jakobs, T.C. (2022). Microglia depletion exacerbates retinal ganglion cell loss in a mouse model of glaucoma. Exp. Eye Res. *225*, 109273. https://doi.org/10.1016/j.exer.2022.109273.

39. Norris, G.T., Smirnov, I., Filiano, A.J., Shadowen, H.M., Cody, K.R., Thompson, J.A., Harris, T.H., Gaultier, A., Overall, C.C., and Kipnis, J. (2018). Neuronal integrity and complement control synaptic material clearance by microglia after CNS injury. J. Exp. Med. *215*, 1789–1801. https://doi.org/10.1084/jem.20172244.

40. Lei, F., Cui, N., Zhou, C., Chodosh, J., Vavvas, D.G., and Paschalis, E.I. (2020). CSF1R inhibition by a small-molecule inhibitor is not microglia specific; affecting hematopoiesis and the function of macrophages. Proc. Natl. Acad. Sci. USA *117*, 23336–23338. https://doi.org/10.1073/pnas.1922788117.

41. Hammond, T.R., Robinton, D., and Stevens, B. (2018). Microglia and the Brain: Complementary Partners in Development and Disease. Annu. Rev. Cell Dev. Biol. *34*, 523–544. https://doi.org/10.1146/annurev-cellbio-100616-060509.

42. Zhang, S., Meng, R., Jiang, M., Qing, H., and Ni, J. (2024). Emerging Roles of Microglia in Blood-brain Barrier Integrity in Aging and Neurodegeneration. Curr. Neuropharmacol. *22*, 1189–1204. https://doi.org/10.2174/1570159X21666230203103910.

43. Takata, F., Nakagawa, S., Matsumoto, J., and Dohgu, S. (2021). Blood-Brain Barrier Dysfunction Amplifies the Development of Neuroinflammation: Understanding of Cellular Events in Brain Microvascular Endothelial Cells for Prevention and Treatment of BBB Dysfunction. Front. Cell. Neurosci. *15*, 661838. https://doi.org/10.3389/fncel.2021.661838.

44. Mastorakos, P., Mihelson, N., Luby, M., Burks, S.R., Johnson, K., Hsia, A.W., Witko, J., Frank, J.A., Latour, L., and McGavern, D.B. (2021). Temporally distinct myeloid cell responses mediate damage and repair after cerebrovascular injury. Nat. Neurosci. *24*, 245–258. https://doi.org/10.1038/s41593-020-00773-6.

45. Liu, J., Tsang, J.K.W., Fung, F.K.C., Chung, S.K., Fu, Z., and Lo, A.C.Y. (2022). Retinal microglia protect against vascular damage in a mouse model of retinopathy of prematurity. Front. Pharmacol. *13*, 945130. https://doi.org/10.3389/fphar.2022.945130.

46. Cunha-Vaz, J., Bernardes, R., and Lobo, C. (2011). Blood-retinal barrier. Eur. J. Ophthalmol. *21* (*Suppl 6*), S3–S9. https://doi.org/10.5301/EJO.2010.6049.

47. Rust, R., Grönnert, L., Dogançay, B., and Schwab, M.E. (2019). A Revised View on Growth and Remodeling in the Retinal Vasculature. Sci. Rep. *9*, 3263. https://doi.org/10.1038/s41598-019-40135-2.

48. Taylor, A.W. (2009). Ocular immune privilege. Eye *23*, 1885–1889. https://doi.org/10.1038/eye.2008.382.

49. Hasenberg, A., Hasenberg, M., Männ, L., Neumann, F., Borkenstein, L., Stecher, M., Kraus, A., Engel, D.R., Klingberg, A., Seddigh, P., et al. (2015). Catchup: a mouse model for imaging-based tracking and modulation of neutrophil granulocytes. Nat. Methods *12*, 445–452. https://doi.org/10.1038/nmeth.3322.

50. Grieshaber-Bouyer, R., Radtke, F.A., Cunin, P., Stifano, G., Levescot, A., Vijaykumar, B., Nelson-Maney, N., Blaustein, R.B., Monach, P.A., and Nigrovic, P.A.; ImmGen Consortium (2021). The neutrotime transcriptional

signature defines a single continuum of neutrophils across biological compartments. Nat. Commun. *12*, 2856. https://doi.org/10.1038/s41467-021-22973-9.

51. McLenachan, S., Magno, A.L., Ramos, D., Catita, J., McMenamin, P.G., Chen, F.K., Rakoczy, E.P., and Ruberte, J. (2015). Angiography reveals novel features of the retinal vasculature in healthy and diabetic mice. Exp. Eye Res. *138*, 6–21. https://doi.org/10.1016/j.exer.2015.06.023.
52. Nourshargh, S., and Alon, R. (2014). Leukocyte migration into inflamed tissues. Immunity *41*, 694–707. https://doi.org/10.1016/j.immuni.2014.10.008.
53. Phillipson, M., Heit, B., Colarusso, P., Liu, L., Ballantyne, C.M., and Kubes, P. (2006). Intraluminal crawling of neutrophils to emigration sites: a molecularly distinct process from adhesion in the recruitment cascade. J. Exp. Med. *203*, 2569–2575. https://doi.org/10.1084/jem.20060925.
54. Lamers, C., Plüss, C.J., and Ricklin, D. (2021). The Promiscuous Profile of Complement Receptor 3 in Ligand Binding, Immune Modulation, and Pathophysiology. Front. Immunol. *12*, 662164. https://doi.org/10.3389/fimmu.2021.662164.
55. Hyun, Y.M., Choe, Y.H., Park, S.A., and Kim, M. (2019). LFA-1 (CD11a/CD18) and Mac-1 (CD11b/CD18) distinctly regulate neutrophil extravasation through hotspots I and II. Exp. Mol. Med. *51*, 1–13. https://doi.org/10.1038/s12276-019-0227-1.
56. Park, K.K., Liu, K., Hu, Y., Smith, P.D., Wang, C., Cai, B., Xu, B., Connolly, L., Kramvis, I., Sahin, M., and He, Z. (2008). Promoting axon regeneration in the adult CNS by modulation of the PTEN/mTOR pathway. Science *322*, 963–966. https://doi.org/10.1126/science.1161566.
57. Zhao, X.F., Huffman, L.D., Hafner, H., Athaiya, M., Finneran, M.C., Kalinski, A.L., Kohen, R., Flynn, C., Passino, R., Johnson, C.N., et al. (2022). The injured sciatic nerve atlas (iSNAT), insights into the cellular and molecular basis of neural tissue degeneration and regeneration. Elife *11*, e80881. https://doi.org/10.7554/eLife.80881.
58. Xie, L., Yin, Y., and Benowitz, L. (2021). Chemokine CCL5 promotes robust optic nerve regeneration and mediates many of the effects of CNTF gene therapy. Proc. Natl. Acad. Sci. USA *118*, e2017282118. https://doi.org/10.1073/pnas.2017282118.
59. Xu, Q., Zhao, W., Yan, M., and Mei, H. (2022). Neutrophil reverse migration. J. Inflamm. *19*, 22. https://doi.org/10.1186/s12950-022-00320-z.
60. Stevens, B., Allen, N.J., Vazquez, L.E., Howell, G.R., Christopherson, K.S., Nouri, N., Micheva, K.D., Mehalow, A.K., Huberman, A.D., Stafford, B., et al. (2007). The classical complement cascade mediates CNS synapse elimination. Cell *131*, 1164–1178. https://doi.org/10.1016/j.cell.2007.10.036.
61. Peterson, S.L., Li, Y., Sun, C.J., Wong, K.A., Leung, K.S., de Lima, S., Hanovice, N.J., Yuki, K., Stevens, B., and Benowitz, L.I. (2021). Retinal Ganglion Cell Axon Regeneration Requires Complement and Myeloid Cell Activity within the Optic Nerve. J. Neurosci. *41*, 8508–8531. https://doi.org/10.1523/JNEUROSCI.0555-21.2021.
62. Hong, S., Beja-Glasser, V.F., Nfonoyim, B.M., Frouin, A., Li, S., Ramakrishnan, S., Merry, K.M., Shi, Q., Rosenthal, A., Barres, B.A., et al. (2016). Complement and microglia mediate early synapse loss in Alzheimer mouse models. Science *352*, 712–716. https://doi.org/10.1126/science.aad8373.
63. Murakami, Y., Ishikawa, K., Nakao, S., and Sonoda, K.H. (2020). Innate immune response in retinal homeostasis and inflammatory disorders. Prog. Retin. Eye Res. *74*, 100778. https://doi.org/10.1016/j.preteyeres.2019.100778.
64. Sorvillo, N., Cherpokova, D., Martinod, K., and Wagner, D.D. (2019). Extracellular DNA NET-Works With Dire Consequences for Health. Circ. Res. *125*, 470–488. https://doi.org/10.1161/CIRCRESAHA.119.314581.
65. Strecker, J.K., Schmidt, A., Schäbitz, W.R., and Minnerup, J. (2017). Neutrophil granulocytes in cerebral ischemia - Evolution from killers to key players. Neurochem. Int. *107*, 117–126. https://doi.org/10.1016/j.neuint.2016.11.006.
66. Jerome, A.D., Atkinson, J.R., McVey Moffatt, A.L., Sepeda, J.A., Segal, B.M., and Sas, A.R. (2022). Characterization of Zymosan-Modulated Neutrophils With Neuroregenerative Properties. Front. Immunol. *13*, 912193. https://doi.org/10.3389/fimmu.2022.912193.
67. Cahilog, Z., Zhao, H., Wu, L., Alam, A., Eguchi, S., Weng, H., and Ma, D. (2020). The Role of Neutrophil NETosis in Organ Injury: Novel Inflammatory Cell Death Mechanisms. Inflammation *43*, 2021–2032. https://doi.org/10.1007/s10753-020-01294-x.
68. Scholz, M., Cinatl, J., Schädel-Höpfner, M., and Windolf, J. (2007). Neutrophils and the blood-brain barrier dysfunction after trauma. Med. Res. Rev. *27*, 401–416. https://doi.org/10.1002/med.20064.
69. Wang, H., Hong, L.J., Huang, J.Y., Jiang, Q., Tao, R.R., Tan, C., Lu, N.N., Wang, C.K., Ahmed, M.M., Lu, Y.M., et al. (2015). P2RX7 sensitizes Mac-1/ICAM-1-dependent leukocyte-endothelial adhesion and promotes neurovascular injury during septic encephalopathy. Cell Res. *25*, 674–690. https://doi.org/10.1038/cr.2015.61.
70. Cruz Hernández, J.C., Bracko, O., Kersbergen, C.J., Muse, V., Haft-Javaherian, M., Berg, M., Park, L., Vinarcsik, L.K., Ivasyk, I., Rivera, D.A., et al. (2019). Neutrophil adhesion in brain capillaries reduces cortical blood flow and impairs memory function in Alzheimer's disease mouse models. Nat. Neurosci. *22*, 413–420. https://doi.org/10.1038/s41593-018-0329-4.
71. Bracko, O., Njiru, B.N., Swallow, M., Ali, M., Haft-Javaherian, M., and Schaffer, C.B. (2020). Increasing cerebral blood flow improves cognition into late stages in Alzheimer's disease mice. J. Cerebr. Blood Flow Metabol. *40*, 1441–1452. https://doi.org/10.1177/0271678X19873658.
72. Manda-Handzlik, A., and Demkow, U. (2019). The Brain Entangled: The Contribution of Neutrophil Extracellular Traps to the Diseases of the Central Nervous System. Cells *8*, 1477. https://doi.org/10.3390/cells8121477.
73. Allen, C., Thornton, P., Denes, A., McColl, B.W., Pierozynski, A., Monestier, M., Pinteaux, E., Rothwell, N.J., and Allan, S.M. (2012). Neutrophil cerebrovascular transmigration triggers rapid neurotoxicity through release of proteases associated with decondensed DNA. J. Immunol. *189*, 381–392. https://doi.org/10.4049/jimmunol.1200409.
74. Kolaczkowska, E., and Kubes, P. (2013). Neutrophil recruitment and function in health and inflammation. Nat. Rev. Immunol. *13*, 159–175. https://doi.org/10.1038/nri3399.
75. McColl, B.W., Rothwell, N.J., and Allan, S.M. (2008). Systemic inflammation alters the kinetics of cerebrovascular tight junction disruption after experimental stroke in mice. J. Neurosci. *28*, 9451–9462. https://doi.org/10.1523/JNEUROSCI.2674-08.2008.
76. Zenaro, E., Pietronigro, E., Della Bianca, V., Piacentino, G., Marongiu, L., Budui, S., Turano, E., Rossi, B., Angiari, S., Dusi, S., et al. (2015). Neutrophils promote Alzheimer's disease-like pathology and cognitive decline via LFA-1 integrin. Nat. Med. *21*, 880–886. https://doi.org/10.1038/nm.3913.
77. Davalos, D., Ryu, J.K., Merlini, M., Baeten, K.M., Le Moan, N., Petersen, M.A., Deerinck, T.J., Smirnoff, D.S., Bedard, C., Hakozaki, H., et al. (2012). Fibrinogen-induced perivascular microglial clustering is required for the development of axonal damage in neuroinflammation. Nat. Commun. *3*, 1227. https://doi.org/10.1038/ncomms2230.
78. Rajarathnam, K., Schnoor, M., Richardson, R.M., and Rajagopal, S. (2019). How do chemokines navigate neutrophils to the target site: Dissecting the structural mechanisms and signaling pathways. Cell. Signal. *54*, 69–80. https://doi.org/10.1016/j.cellsig.2018.11.004.
79. Sekheri, M., Othman, A., and Filep, J.G. (2021). β2 Integrin Regulation of Neutrophil Functional Plasticity and Fate in the Resolution of Inflammation. Front. Immunol. *12*, 660760. https://doi.org/10.3389/fimmu.2021.660760.
80. Xia, Y., Vetvicka, V., Yan, J., Hanikýrová, M., Mayadas, T., and Ross, G.D. (1999). The beta-glucan-binding lectin site of mouse CR3 (CD11b/CD18) and its function in generating a primed state of the receptor that mediates cytotoxic activation in response to iC3b-opsonized target cells. J. Immunol. *162*, 2281–2290. https://pubmed.ncbi.nlm.nih.gov/9973505.
81. Byrd, A.S., O'Brien, X.M., Johnson, C.M., Lavigne, L.M., and Reichner, J.S. (2013). An extracellular matrix-based mechanism of rapid neutrophil

extracellular trap formation in response to Candida albicans. J. Immunol. *190*, 4136–4148. https://doi.org/10.4049/jimmunol.1202671.

82. Clauser, K.R., Baker, P., and Burlingame, A.L. (1999). Role of accurate mass measurement (+/- 10 ppm) in protein identification strategies employing MS or MS/MS and database searching. Anal. Chem. *71*, 2871–2882. https://doi.org/10.1021/ac9810516.

83. Guan, S., Price, J.C., Prusiner, S.B., Ghaemmaghami, S., and Burlingame, A.L. (2011). A data processing pipeline for mammalian proteome dynamics studies using stable isotope metabolic labeling. Mol. Cell. Proteomics *10*, M111.010728. https://doi.org/10.1074/mcp.M111.010728.

84. Elmore, M.R.P., Najafi, A.R., Koike, M.A., Dagher, N.N., Spangenberg, E.E., Rice, R.A., Kitazawa, M., Matusow, B., Nguyen, H., West, B.L., and Green, K.N. (2014). Colony-stimulating factor 1 receptor signaling is necessary for microglia viability, unmasking a microglia progenitor cell in the adult brain. Neuron *82*, 380–397. https://doi.org/10.1016/j.neuron.2014.02.040.

85. Dickendesher, T.L., Baldwin, K.T., Mironova, Y.A., Koriyama, Y., Raiker, S.J., Askew, K.L., Wood, A., Geoffroy, C.G., Zheng, B., Liepmann, C.D., et al. (2012). NgR1 and NgR3 are receptors for chondroitin sulfate proteoglycans. Nat. Neurosci. *15*, 703–712. https://doi.org/10.1038/nn.3070.

86. Hofer, T., Tangkeangsirisin, W., Kennedy, M.G., Mage, R.G., Raiker, S.J., Venkatesh, K., Lee, H., Giger, R.J., and Rader, C. (2007). Chimeric rabbit/human Fab and IgG specific for members of the Nogo-66 receptor family selected for species cross-reactivity with an improved phage display vector. J. Immunol. Methods *318*, 75–87. https://doi.org/10.1016/j.jim.2006.10.007.

87. Kalinski, A.L., Yoon, C., Huffman, L.D., Duncker, P.C., Kohen, R., Passino, R., Hafner, H., Johnson, C., Kawaguchi, R., Carbajal, K.S., et al. (2020). Analysis of the immune response to sciatic nerve injury identifies efferocytosis as a key mechanism of nerve debridement. Elife *9*, e60223. https://doi.org/10.7554/eLife.60223.

88. Marsh, S.E., Walker, A.J., Kamath, T., Dissing-Olesen, L., Hammond, T.R., de Soysa, T.Y., Young, A.M.H., Murphy, S., Abdulraouf, A., Nadaf, N., et al. (2022). Dissection of artifactual and confounding glial signatures by single-cell sequencing of mouse and human brain. Nat. Neurosci. *25*, 306–316. https://doi.org/10.1038/s41593-022-01022-8.

STAR★METHODS

KEY RESOURCES TABLE

REAGENT or RESOURCE	SOURCE	IDENTIFIER
Antibodies		
anti-Ly6G, clone 1A8 (blocking antibody)	BioXcell	BE0075-1; RRID: AB_1107721
anti-CD11b, clone M1/70 (blocking antibody)	Invitrogen	16-0112-82; RRID: AB_468884
IgG2a (isotype control)	BioXCell	BE0089; RRID: AB_1107769
anti-Ly6G-APC-Cy7	BD Biosciences	560600; RRID: AB_1727561
Rat IgG2a Isotype Control	ThermoFisher	47-4321-82; RRID: AB_1271997
Annexin V – APC	BD Biosciences	561012; RRID: AB_2034024
anti-Ly6C – FITC	BD Biosciences	553104; RRID: AB_394628
Rat IgM – FITC	BD Biosciences	553942; RRID: AB_479631
anti-CD45 – e450	ThermoFisher	48-0451-82; RRID: AB_1518806
Rat IgG2b Isotype Control – e450	ThermoFisher	48-4031-82; RRID: AB_1272017
anti-CX3CR1 – PE	R&D Systems	FAB5825P-100
Goat IgG Isotype Control – PE	R&D Systems	IC108P
anti-CD11b-PE-Cy7	ThermoFisher	25-0112-82; RRID: AB_469588
Rat IgG2b Isotype Control – PE-Cy7	ThermoFisher	25-4031-82; RRID: AB_891624
anti-CD11c – PerCP – Cy5.5	ThermoFisher	45-0114-82; RRID: AB_925727
Arm Ham IgG Isotype Control – PerCP-Cy5.5	ThermoFisher	45-4888-80; RRID: AB_906260
CD16/CD32 Monoclonal Antibody, eBioscience (Fc Block)	ThermoFisher	14-0161-85; RRID: AB_467134
Rabbit anti-Iba1	Wako	019–19741; RRID: AB_839504
Rat anti-CD31	Biolegend	102502; RRID: AB_312909
Goat anti-CD31	R&D Systems	AF3628; RRID: AB_2161028
Rabbit anti-RBPMS	PhosphoSolutions	1830-RBPMS; RRID: AB_2492225
Chemicals, peptides, and recombinant proteins		
Actinomycin D	Sigma-Aldrich	A1410
Tamoxifen	Sigma-Aldrich	T5648
Cholera Toxin Subunit B (CTB)-555 conjugate	Invitrogen	C22843
Fluorescein sodium salt	Sigma-Aldrich	46960
Trichloroacetic acid (TCA)	Sigma-Aldrich	76039
Fixable Viability - AmCyan	Invitrogen	65-0866-14
Collagenase II	Worthington	LS004176
Protease Inhibitor Cocktail	Sigma-Aldrich	P8340
Guanidinium Hydrochloride	Sigma-Aldrich	G3272
Ammonium bicarbonate	Sigma-Aldrich	09830
Tris(2-carboxyethyl)phosphine	Sigma-Aldrich	C4706
Iodoacetamide	Sigma-Aldrich	I6125
Lysyl Endopeptidase, Mass Spectrometry Grade (Lys-C)	FUJIFILM Wako	125–05061
Trypsin MS grade	ThermoFisher	90057
Formic acid	Sigma-Aldrich	27001
OMIX C18 pipette tips	Agilent	A57003100K
TMT 10plex kit	ThermoFisher	PI90110
Triethylammonium bicarbonate (TEAB)	Sigma-Aldrich	18597
C18 Sep-Pak cartridge	Waters	WAT051910
Gemini 3u C18 110A 100 × 1.0 mm column	Phenomenex	00D-4439-A0

(*Continued on next page*)

Continued

REAGENT or RESOURCE	SOURCE	IDENTIFIER
PepMap RSLC C18 EasySpray column	ThermoFisher	ES903
Orbitrap Exploris 480	ThermoFisher	BRE725533
Deposited data		
Single cell RNA-seq datasets (fastq files and Seurat objects) of ocular immune cells of WT and *Itgam*−/− mice	Gene Expression Omnibus (GEO) database	GSE244627
Proteomics data of the WT and *Itgam*−/− mouse vitreous	ProteomeXchange via the PRIDE database	PXD045885
Experimental models: Organisms/strains		
Mouse: Csf1r flox/flox	The Jackson Laboratory	Stock# 021212
Mouse: Tmem119-creER	The Jackson Laboratory	Stock# 031820
Mouse: LysM-cre	The Jackson Laboratory	Stock# 004781
Mouse: ROSA26-EGFP	The Jackson Laboratory	Stock# 004077
Mouse: Itgam	The Jackson Laboratory	Stock# 003991
Mouse: C1q	The Jackson Laboratory	Stock# 031675
Mouse: Catchup (Ly6g reporter)	Dr. Ki-Wook Kim	Hasenberg et al.[49]
Mouse: C3	The Jackson Laboratory	Stock# 029661
Mouse: Arg1-YFP	The Jackson Laboratory	Stock# 015857
Mouse: ROSA26-mTdtomato	The Jackson Laboratory	Stock# 007914
Mouse: Tmem119-eGFP	The Jackson Laboratory	Stock# 031823
Oligonucleotides		
Csf1r forward: CATGGCTGTGGCCTAGAGA	The Jackson Laboratory	Stock# 021212
Csf1r reverse: GGACTAGCCACCATGTCTCC	The Jackson Laboratory	Stock# 021212
Tmem119-creER WT forward: CAGTATGTGGGGTCACTGAAGA	The Jackson Laboratory	Stock# 031820
Tmem119-creER mutant forward: ATCGCATTCCTTGCAAAAGT	The Jackson Laboratory	Stock# 031820
Tmem119-creER common: ACTTGGGGAGATGTTTCCTG	The Jackson Laboratory	Stock# 031820
LysM-cre WT Reverse: GTCACTCACTGCTCCCCTGT	The Jackson Laboratory	Stock# 004781
LysM-cre Mutant Reverse: ACCGGTAATGCAGGCAAAT	The Jackson Laboratory	Stock# 004781
LysM-cre Common: AAGGAGGGACTTGGAGGATG	The Jackson Laboratory	Stock# 004781
ROSA26-EGFP WT Forward: AAGGGAGCTGCAGTGGAGTA	The Jackson Laboratory	Stock# 004077
ROSA26-EGFP WT Reverse: GAGCGGGAGAAATGGATATG	The Jackson Laboratory	Stock# 004077
ROSA26-EGFP Mutant Forward: GATCACTCACGGCATGGAC	The Jackson Laboratory	Stock# 004077
ROSA26-EGFP Mutant Reverse: CGGGCCTCTTCGCTATTAC	The Jackson Laboratory	Stock# 004077
Itgam WT Reverse: CCTTTGATCTCTCCCCACCT	The Jackson Laboratory	Stock# 003991
Itgam Mutant Reverse: TGATTCCCACTTTGTGGTTC	The Jackson Laboratory	Stock# 003991
Itgam Common: TGTTTTTACCCCTCCCTCCT	The Jackson Laboratory	Stock# 003991
C1q WT Reverse: CCTCTCTGAGCCTCTGCTTC	The Jackson Laboratory	Stock# 031675
C1q Mutant Reverse: CCAGAAAGTGCTTAAAGAAACCA	The Jackson Laboratory	Stock# 031675
C1q Common: AGGACCCTCATGCTGATTTG	The Jackson Laboratory	Stock# 031675
C3 WT: GGTTGCAGCAGTCTATGAAGG	The Jackson Laboratory	Stock# 029661
C3 Mutant: GCCAGAGGCCACTTGTGTAG	The Jackson Laboratory	Stock# 029661
C3 Common: ATCTTGAGTGCACCAAGCC	The Jackson Laboratory	Stock# 029661
Tmem119-EGFP WT Forward: CAGTATGTGGGGTCACTGAAGA	The Jackson Laboratory	Stock# 031823
Tmem119-EGFP Mutant Forward: AGCGCGATCACATGGTCCTG	The Jackson Laboratory	Stock# 031823
Tmem119-EGFP Common: ACTTGGGGAGATGTTTCCTG	The Jackson Laboratory	Stock# 031823

(*Continued on next page*)

Continued

REAGENT or RESOURCE	SOURCE	IDENTIFIER
Software and algorithms		
MF_Axon_Count_1.0, R software written for interval-based quantification of regenerating axons in the optic nerve	R software	https://zenodo.org/records/10650620
CellRanger	10X Genomics, Inc	Version 7.0.1
Seurat	Satija Lab–New York Genome Center	Version 4.1.1
R	r-project.org	Version 4.1.2
STRING-DB.org	String Consortium	Version 12.0
Zen Blue	Zeiss	Version 3.5
FIJI	ImageJ	Version 2.1.0
LI-COR Image Studio	LI-COR Biosciences	Version 5.2.5
GraphPad Prism	GraphPad software Inc.	Version 9
FlowJo	BD Biosciences	Version 10
ProteinProspector	Clauser et al.[82]	https://prospector.ucsf.edu/
PAVA	Guan et al.[83]	N/A
Other		
Particulate β(1,3)(1,6) glucan	ImmunoResearch, Inc	IRI-1501
Soluble β(1,3)(1,6) glucan	ImmunoResearch, Inc	IRI-1800
Csf1R inhibitor	Plexxikon, Inc	PLX5622
Proteome Profiler Mouse XL Cytokine Kit	R&D Systems	ARY028
Chromium Next GEM Single Cell 3′ Reagent kit v3.1	10X Genomics, Inc	1000268
10X Genomics Chromium Controller	10X Genomics, Inc	GCG-SR-1
Dual Index Kit TT Set A	10X Genomics, Inc	1000125
Chromium Next GEM Chip G Single Cell kit	10X Genomics, Inc	1000127
Dynabeads MyOne Silane	10X Genomics, Inc	2000048
SPRIselect reagent kit	Beckman Coulter Life Sciences	B23318
High Select Top14 Depletion Resin	Thermo Scientific	A36369
High Select Top14 Depletion Resin	Thermo Scientific	A36372
MACS MultiStand	Miltenyi Biotec	130-042-303
MidiMACS Separator	Miltenyi Biotec	130-042-302
LS Columns	Miltenyi Biotec	130-042-401
CD45 MicroBeads, mouse	Miltenyi Biotec	130-052-301
Microtainer Blood Collection Tubes	BD Biosciences	365974
ACK lysis buffer	Gibco	A10492-01
Falcon 40 μm cell strainer	Corning	352340
Phosphate buffered saline (PBS)	Gibco	10010–023
Fetal Bovine Serum - Premium	R&D Systems	S11150
Amicon Ultra Centrifugal Filter, 30 kDa MWCO	Sigma-Aldrich	UFC8030
Pierce BCA Protein Assay Kits	Thermo Scientific	23225

RESOURCE AVAILABILITY

Lead contact

Further information and requests for resources and reagents should be directed to and will be fulfilled by the lead contact, Roman Giger (rgiger@umich.edu).

Materials availability

Request for resources and reagents should be directed to the lead contact. This study did not generate new unique reagents.

Data and code availability

- New generated datasets, including scRNAseq of ocular immune cells, and the vitreal proteome of WT and *Itgam*−/− mice. These datasets are freely available. All scRNA-seq datasets (fastq files and Seurat objects) are available online through the Gene Expression Omnibus (GEO) database https://www.ncbi.nlm.nih.gov/geo under the accession number GSE244627.
- Proteomics data of the WT and *Itgam*−/− mouse vitreous are available through ProteomeXchange via the PRIDE database under the identifier PXD045885.
- Custom code for quantification of regenerated axons in nerve sections is freely available through Github: https://github.com/mcfinner/MF_Axon_Count_1.0
- Any additional information required to reanalyze the data reported in this work is available from the lead contact upon request.

EXPERIMENTAL MODEL AND STUDY PARTICIPANT DETAILS

Mice

All procedures involving mice were approved by the Institutional Animal Care and Use Committee at the University of Michigan (Protocol# PRO00011554) and performed in accordance with guidelines developed by the National Institutes of Health. Adult (8–16 week-old) male and female mice, at an ~ 1:1 ratio, on a C57BL/6 background were used throughout the study. *Csf1r f/f* mice were crossed with *Tmem119-CreERT2* or *LysM-Cre* to generate *Csf1r f/f;Tmem119-CreERT2* and *Csf1r f/f;LysM-Cre* conditional mutants. *Tmem119-CreERT2* and *LysM-Cre* were crossed with *ROSA26-EGFP* reporter mice to evaluate recombination efficiency and specificity. In addition, we used *Itgam*$^{-/-}$, *C1q*$^{-/-}$, and *C3*$^{-/-}$ mice. *Catchup*$^{+/+}$ homozygous and *Catchup*$^{+/-}$ heterozygous mice (*Ly6g-cre;Rfp*) were backcrossed onto *ROSA26-mTdtomato* reporters on a C57BL/6 background and used for lineage tracing of Ly6G^{+} neutrophils. In addition, we employed *Arg1-eYFP* reporter mice and *Tmem119-eGFP* reporter for cell type identification. Mice were housed under a 12 h light/dark cycle with regular chow and water *ad libitum* unless indicated otherwise. For genotyping, ear biopsies were collected, and genomic DNA extracted by boiling in 100 μL alkaline lysis buffer (25 mM NaOH and 0.2 mM EDTA in ddH_2O) for 30 min. The pH was neutralized with 100 μL of 40 mM Tris-HCl (pH 5.5). For PCR, 1–5 μL of gDNA was mixed with 0.4 μL of 10 mM dNTP mix (Promega, C1141, Madison, WI), 1 μL of 25 mM $MgCl_2$, 4 μL of 5X Green GoTaq Buffer (Promega, M791A), 0.2 μL of GoTaq DNA polymerase (Promega, M3005), 0.5 μL of each PCR primer stock (20 μM each), and ddH_2O was added to a total volume of 20 μL. PCR primers were purchased from *Integrated DNA Technologies*.

METHOD DETAILS

Approximately equal numbers of male and female mice were used for all our studies. Cohorts of mice were randomly assigned to experimental groups or controls. All surgeries were carried out at the University of Michigan Medical School in a specifically designated surgical suite. For optic nerve regeneration studies, 8–15 mice were analyzed per experimental group. For blinded quantification of axon regeneration, de-identified images of optic nerves were provided to a lab member who used in-house developed custom code (see below) for unbiased quantification of axon length and number.

Microglia ablation

For pharmacological ablation, male and female mice were fed with chow containing the Csf1R inhibitor PLX5622. The PLX5622 compound was formulated in AIN-76A chow by Research Diets at a dose of 1,200 p.p.m. (1,200 mg of PLX5622 per kg chow). Mice were PLX5622-fed or control AIN-76A-fed (without PLX5622) for two weeks and then subjected to optic nerve injury. Mice were kept on the same diet until optic nerves and eyes were harvested.[84] For genetic ablation of microglia, we generated *Csf1r f/f;Tmem119-CreERT2* mice and to assess recombination efficiency we generated *ROSA26-EGFP;Tmem119-CreERT2* mice. Adult mice were treated with tamoxifen dissolved in corn oil at 20 mg/mL and injected intraperitoneally at 75 mg/kg. Mice were injected once every 24 h for 5 consecutive days, then every third day until sacrifice.

Optic nerve surgery and intra-ocular injections

Optic nerve surgeries and intraocular injections were carried out as described previously.[85] Briefly, mice were deeply anesthetized with a mixture of ketamine (120 mg/kg) and xylazine (10 mg/kg). Buprenorphine (0.1 mg/kg) was given as an analgesic. Sterile ophthalmic lubricant was applied to prevent damage to the cornea during the procedure. The optic nerve was crushed 1mm behind the eyeball for 10 s with curved #5 forceps. Particulate or soluble β(1–3)-(1–6) glucan, (IRI-1501 or IRI-1800, respectively) were prepared from *s. cerevisiae* as GMP grade, and provided under a collaborative research agreement with ImmunoResearch Inc. IRI-1501 and IRI-1800 were concentrated through a spin column (Amicon Ultra Centrifugal Filter, 30 kDa MWCO; Sigma #UFC8030) and injected at the final concentration of 25 mg/mL. For intra-ocular (i.o.) injections, 1–2 μL of β-glucan was injected into the posterior chamber of the eye using a 33-gauge beveled needle immediately following retro-orbital ONC. As vehicle control, 1–2 μL of PBS were injected. For RGC axon anterograde tracing, conjugated cholera toxin subunit B (CTB-555 conjugate; Invitrogen #C22843) was injected into the eye (2 μL of a 2 mg/mL stock solution) 2d before mice were sacrificed and optic nerves harvested. For all i.o. injections, the needle was angled to minimize risk of puncturing the ocular lens.

Antibody treatment

Rat anti-Ly6G antibody (clone 1A8), anti-CD11b (clone M1/70), and isotype control IgG2a were administered intraperitoneally (0.1 mL/mouse at a concentration of 1 mg/mL) starting at 1 day before optic nerve crush, at the time of optic nerve crush, and then every 24hr for the first 72 h post ONC.

Flow cytometry

Mice were euthanized and perfused transcardially with ice-cold PBS for 5 min. Cardiac blood was collected from the right atrium immediately after starting the perfusion into an EDTA coated tube (BD Biosciences #365974). Blood samples were subjected to 3 rounds of ACK lysis buffer (Gibco #A10492-01) treatment to remove red blood cells and then filtered through a 40 μm cell strainer (Corning #352340). Eyes were enucleated and transferred to a small Petri dish (30 mm × 15 mm) with 1mL cold FACS buffer (PBS with 2% FBS). Eyes were then dissected by cutting around the cornea, removing the lens, and extracting the retinas. The retinas were rinsed with FACS buffer and transferred to a clean tube. Vitreous was collected, mixed with FACS buffer, and filtered through a 40 μm cell strainer. Retinas were transferred into 1 mL of 1 mg/mL collagenase II (Worthington #LS004176) and digested at 37°C with agitation every 10 min and 20x trituration every 25 min for 50 min total. Digestion was stopped with FACS buffer and samples were centrifuged to pellet cells and undigested retina. Retinal cells were passed through a 40 μm cell strainer and any remaining undigested tissue gently massaged through the filter with a 5 mL syringe plunger. Samples were stained with fixed viability dye (Invitrogen #65-0866-14) and blocked with anti-CD16/32 (ThermoFisher #14-0161-85), followed by staining with antibody cocktails to identify immune cells ($CD45^+$), microglia ($CD45^+$, CD11b+, CX3CR1+), myeloid cells ($CD45^+$, CD11b+, CX3CR1-), neutrophils ($CD45^+$, CD11b+, CX3CR1-, Ly6G+), dendritic cells ($CD45^+$, CD11b+, CX3CR1-, Ly6G-, CD11c+), monocytes and macrophages ($CD45^+$, CD11b+, CX3CR1-, Ly6G-, CD11c-, Ly6Chigh, Ly6Clow, and Ly6C-). Cells were also stained with Annexin V to identify apoptotic cells expressing phosphatidylserine on their surface. Data were acquired using a FACSCanto II (BD Biosciences) flow cytometer and analyzed with FlowJo software as described previously.[30] For details on gating strategies, see Figure S4.

Optic nerve analysis

Mice were euthanized with an overdose of xylazine/ketamine and transracially perfused for 5 min with ice-cold PBS followed by 5 min with freshly prepared ice-cold 4% paraformaldehyde in PBS. Retinas and optic nerves were harvested and postfixed for 1h in ice-cold PFA (4%) in PBS and then transferred to 30% sucrose in PBS overnight. Optic nerves were embedded and frozen in OCT and then cryosectioned longitudinally at 14 μm. Optic nerve sections were subjected to immunofluorescence labeling.[86] Regenerated axons and stained cells were imaged at 20X with Zeiss Apotome2 microscope equipped with an Axiocam 503 mono camera and ZEN software. At least 2–3 images were taken per nerve for quantification.

Retinal analysis

For retinal flat mount preparation and vascular imaging, mice were slowly perfused transcardially with ice-cold PBS, followed by 4% PFA. Eyes were dissected and post-fixed in 4% PFA for an additional 1hr. For experiments involving *Catchup* reporter mice, mice were not perfused to allow for visualization of neutrophils within the vasculature; instead, eyes were enucleated and directly fixed in 4% PFA for 1hr. Retinas were permeabilized with 2% Triton X-100 in PBS for 1 h at room temp followed by blocking with 10% donkey serum (EMD Millipore #S30-100ML) for 1 h at room temp. Retinas were incubated with primary antibodies diluted in PBST (PBS/0.05% Tween 20) with 5% donkey serum for 3d. Antibodies included Iba1 (Rabbit, Wako #019–19741), CD31 (Rat, Biolegend #102502; Goat, R&D Systems #AF3628), and RBPMS (Rabbit, Abcam #194213). Retinas were then washed with PBST and incubated with secondary antibodies diluted in PBST with 5% donkey serum for 2 h at room temp. Retinas were mounted with prolong-gold mounting media (Invitrogen #P36930) and imaged at 20X with Zeiss Apotome2 microscope using ZEN software.

Assessment of BRB integrity

Sodium fluorescein (NaFI, Sigma #C22843) was dissolved in PBS by vortexing, then 100 μL was administered intraperitoneally at 10% (wt/vol). After 1 h, 0.2 mL cardiac blood was collected, then mice were perfused with cold PBS for 5 min. Retinas extracted (2 retinas pooled per sample) and homogenized in 100 μL 7.5% trichloroacetic acid (TCA, Sigma #76039) in 5 M NaOH by vortexing and manual pipetting. Homogenates were centrifuged at 10,000g for 5 min and the supernatant collected. Blood was centrifuged at 2000 g for 15min, then 25 μL serum (supernatant) was mixed with 25 μL 15% TCA. This mixture was centrifuged at 10,000 g for 5 min, then 25 μL of the supernatant was collected and mixed with 125 μL 7.5% TCA in 5 M NaOH. Fluorescence was quantified using a microplate reader (SpectraMax, Molecular Devices) with excitation at 485 nm, emission at 530 nm and a gain of 50. The uptake ratio was calculated by dividing the fluorescence of the retina by the fluorescence of the serum.

Multiplex ELISA

Mice were euthanized and transcardially perfused with ice-cold PBS for 5 min and eyes dissected. For each ELISA membrane (Proteome Profiler Mouse XL Cytokine Kit), retinas and vitreous from n = 3 adult mice were harvested and pooled in ice-cold PBS supplemented with 1% protease inhibitor cocktail (Sigma #P8340). Tissues were minced and homogenized in ice-cold 1% Triton X-100 (Sigma #T8787) using a Dounce homogenizer, frozen at −80°C, thawed, and centrifuged at 10,000 x g for 5 min to pellet cellular debris. The protein concentration in the supernatant was determined using the Pierce BCA Protein Assay (Thermo Scientific

#23225), and 200 μg of protein in a final volume of 1.5 mL were used for incubation per ELISA membrane. Membranes were probed and developed according to the manufacturer's instructions. Cytokine signals were detected by X-ray film (Ece Scientific Inc. #E3018), scanned, and quantified using LI-COR Image Studio software version 5.2.5. Signals (pixel-density values) from duplicate spots were averaged and normalized to reference spots in upper-right and left corners and the lower-left corner of the membrane.

scRNA-sequencing

Isolation of ocular immune cells: Mice were euthanized and perfused transcardially with ice-cold PBS for 5 min. Eyes from WT and *Itgam*−/− mice, at 3dpc plus i.o. β-glucan, were enucleated and dissected in ice-cold PBS with actinomycin D (45 μM) to collect retinas and vitreous humor. Retinas were digested in collagenase II (Worthington #LS004176) at 1 mg/mL for 40 min at 37°C. The dissociated retinal cells and vitreal cells were then combined and filtered through a 40 μm cell strainer (Corning #352340). To enrich for immune cells, samples were run over an anti-CD45 magnetic column (Miltenyi #130-052-301). Leukocytes were eluted, centrifuged in a 15 mL conical tube at 300xg for 10 min, and counted. The live/dead ratio was determined using propidium iodine staining and a hemocytometer.[87] For library preparation, we used the Chromium Next GEM Single Cell 3′ Reagent kit v3.1 (Dual Index). Barcoding and library preparation was performed following the manufacturer's protocols. Briefly, to generate single-cell gel-bead-in-emulsion (GEMs) solution, approximately 15,000 cells, in a final volume of 43 μL, were loaded on a Next GEM Chip G (10X Genomics) and processed with the 10X Genomics Chromium Controller. Reverse transcription was performed as follows: 53C for 45 min and 85C for 5 min in a Veriti Thermal Cycler (Applied Biosystems). Next, first-strand cDNA was cleaned with DynaBeads MyOne SILANE (10 X Genomics, 2000048). The amplified cDNA, intermedium products, and final libraries were prepared and cleaned with SPRIselect Regent kit (Beckman Coulter, B23318). A small aliquot of each library was used for quality control to determine fragment size distribution and DNA concentration using a bioanalyzer.[87] Libraries were pooled for sequencing with a NovaSeq 6000 (Illumina) at an estimated depth of 50,000 reads per cell, yielding 2.9 billion reads.

scRNAseq data analysis

Raw scRNAseq datasets were processed using the 10X Genomics CellRanger software version 7.0.1 as described.[57] CellRanger filtered cells were further processed using Seurat version 4.1.1. Cells with fewer than 500 features, more than 200,000 counts, or greater than 15% mitochondrial content were removed. A Shared Nearest Neighbor graph was constructed from the top 20 Principal Components and the Louvain algorithm used with resolution parameter 0.5 to identify 18 clusters. Clusters with photoreceptor markers for rods or cones and bipolar cells were removed prior to downstream analysis. Remaining cells were integrated with our previously described naive mouse peripheral blood mononuclear cells (PBMC) dataset[57] using the Seurat anchor based CCA integration workflow. We used the same dimensional reduction and clustering technique but from 12 Principal Components due to fewer variation sources (non-immune cells removed). This resulted in 13 clusters, and a few modifications were made. Cells in cluster 8 were considered Mac_2 but a subset of the cluster, which expressed *Mki67*, were reclassified as Mac_3. Dendritic Cells (DC) in cluster 9 that did not express *Flt3, Ccr7*, or *Ccl5* were reclassified as MoDC. In a cluster of mixed cells, 50% of which were PBMC cells, those expressing *Cd3g* were labeled as T Cells and those expressing *Bank1* labeled as B Cells, with the majority of B cells originating from the PBMC dataset. Although enzymatic dissociation of retinas was carried out in the presence of actinomycin D (see above), we analyzed myeloid cells for the presence of dissociation associated artifactual gene expression signatures.[88] Mouse CNS activation scores, calculated based on expression of *Fos, Junb, Zfb36, Jun, Hspa1a, Socs3, Rgs1, Egr1, Btg2, Fosb, Hist1h1d, Ier5, Ecrg4, Atf3, Hist1h2ac, Dusp1, Hist1h1e, Folr1*, and *Serpine1*, were absent from ocular monocytes and macrophage populations, providing confidence in the quality of the datasets generated. To perform pathway analysis the top 100–200 enriched markers for a cluster were uploaded to String-db.org's multiple proteins search. FDR p values are reported as shown in the analysis section of the string-db results.

Proteomics of vitreous

In solution digestion: Aliquots of vitreous samples (from n = 8 WT or n = 8 *Itgam*−/− mice) were digested with LysC and trypsin for proteomic analysis, as follows. Samples (20 μg protein) were resuspended at a concentration of 4 mg/mL in a solution containing 8M Guanidinium Hydrochloride (GndHCl; Sigma-Aldrich, Cat #G3272), 100 mM ammonium bicarbonate (Sigma-Aldrich, Cat # 09830) and 10 mM tris(2-carboxyethyl)phosphine (Sigma-Aldrich, Cat #C4706) and incubated for 1h at 56°C. This was followed by addition of 20 mM iodoacetamide (Sigma-Aldrich, Cat #I6125) and a 30-min incubation at room temperature in the dark. The samples were then diluted with 100 mM ammonium bicarbonate to 1M GndHCl and protein concentration 0.5 mg/mL. For digestion, the samples were then added 2% (W/W) Lysyl Endopeptidase, Mass Spectrometry Grade (Lys-C) (FUJIFILM Wako Chemicals U.S.A. Corporation, cat#125–05061) and incubated at 37°C on a rotator overnight. After that, samples were added to 2% (W/W) trypsin MS grade (Pierce-Thermo Fisher, cat# 90057) and digested for 6 additional hours. After this, samples were acidified with formic acid (Sigma-Aldrich, Cat # 27001) to a final concentration of 5% formic, and the digests were then desalted using OMIX C18 pipette tips (Agilent, cat # A57003100K) following the manufacturer's protocol. OMIX eluates were dry-evaporated in preparation for direct "label free" MS analysis or for labeling with tandem mass tag (TMT) reagents for quantitative comparison.

For TMT labeling, digested vitreous proteins were labeled according to the TMT 10plex kit instructions (ThermoFisher Scientific, cat# PI90110). Protein levels in WT and *Itgam*−/− vitreous were compared by TMT in triplicates, using 25 μg of digested protein per TMT channel. Dried pellets of digested samples were resuspended in 100 mM triethylammonium bicarbonate (TEAB; Sigma-Aldrich,

Cat # 18597) pH 8.5 for labeling, and samples in 40 μl TEAB were added 20 μL TMT reagent (25 mg/mL) and incubated for 1 h at room temperature, then 5 μL of 5% hydroxylamine was added to quench excess reagents. After incubating 30 min at room temperature, all 6 labeled samples (n = 3 WT and n = 3 *Itgam*−/−) were combined over 15 mL 0.1% formic acid and desalted using a C18 Sep-Pak cartridge (Waters, cat # WAT051910). The Sep-Pak eluate was dried in preparation for fractionation by high pH reverse phase chromatography. Because of similarity to human proteins, we used High Select Top14 Depletion Resin (Thermo Fisher, cat# A36372) for partial depletion of mouse albumin, fibrinogen, and ApoA.

High pH reverse phase chromatography

Combined, TMT labeled sample was fractionated on an AKTA purifier system utilizing a Phenomenex Gemini 3u C18 110A 100 × 1.0 mm column (cat # 00D-4439-A0), operating at a flow rate of 0.080 mL/min. Buffer A consisted of 20 mM ammonium formate (pH 10), and buffer B consisted of 20 mM ammonium formate in 90% acetonitrile. Gradient details were as follows: 1% to 30% B in 95 min, 30% B to 70% B in 12.5 min, 70% B back down to 1% B in 25 min 0.27 mL fractions were collected, evaporated, and resuspended in 0.1% formic for mass spectrometry analysis.

Mass spectrometry analysis

Peptide digests were resuspended in 0.1% formic acid and injected (approximately 2 μg) to run onto a 2 μm 75 μm × 50 cm PepMap RSLC C18 EasySpray column (Thermo Scientific, cat# ES903). For peptide elution, 3-h water/acetonitrile gradients (2–25% in 0.1% formic acid) were used, at a flow rate of 200 nL/min, for analysis in an Orbitrap Exploris 480 (Thermo Scientific, cat# BRE725533) in positive ion mode. MS spectra were acquired between 375 and 1400 m/z with a resolution of 120000. For each MS spectrum, multiply charged ions over the selected threshold (2E4) were selected for MS/MS in cycles of 3 s with an isolation window of 1.6 m/z. Precursor ions were fragmented by HCD using a relative collision energy of 30. MS/MS spectra were acquired in centroid mode with resolution 30000 from m/z = 120. A dynamic exclusion window was applied which prevented the same m/z from being selected for 30s after its acquisition. For analysis of the TMT experiment, aliquots of 10 non-consecutive chromatographic fractions were run as described above, and Orbitrap Exploris 480 acquisition parameters were adjusted as follows: MS spectra were acquired between 375 and 1500 m/z; isolation window was 0.7 m/z and precursor ions were fragmented by HCD using stepped relative collision energies of 30, 35 and 40 in order to ensure efficient generation of sequence ions as well as TMT reporter ions. MS/MS spectra were acquired in centroid mode with resolution 60000 from m/z = 120.

Peptide and protein identification and quantitation

Peak lists were generated using PAVA in-house software.[83] All generated peak lists were searched against the mouse subset of the SwissProt database (SwissProt.2019.07.31, 17026 entries searched), using Protein Prospector[82] with the following parameters: Enzyme specificity was set as Trypsin, and up to 2 missed cleavages per peptide were allowed. Carbamidomethylation of cysteine residues, and, in the case of TMT labeled samples, TMT10plex labeling of lysine residues and N terminus of the protein were allowed as fixed modifications. N-acetylation of the N terminus of the protein, loss of protein N-terminal methionine, pyroglutamate formation from of peptide N-terminal glutamines, oxidation of methionine was allowed as variable modifications. Mass tolerance was 10 ppm in MS and 30 ppm in MS/MS. The false positive rate was estimated by searching the data using a concatenated database which contains the original SwissProt database, as well as a version of each original entry where the sequence has been randomized. A 1% FDR was permitted at the protein and peptide level. For quantitation only unique peptides were considered; peptides common to several proteins were not used for quantitative analysis. For TMT based quantitation, relative quantization of peptide abundance was performed via calculation of the intensity of reporter ions corresponding to the different TMT labels, present in MS/MS spectra. Intensities were determined by Protein Prospector. Median intensities of the reporter ions (each TMT channel) for all peptide spectral matches (PSMs) were used to normalize individual (sample specific) intensity values. For each PSM, relative abundances were calculated as ratios vs. the average intensity levels in the 3 channels corresponding to control (WT) samples. For total protein relative levels, peptide ratios were aggregated to the protein levels using median values of the log2 ratios. Statistical significance was calculated comparing the values for the 3 technical replicates of WT and *Itgam*−/− samples in the TMT experiment with a 2-tailed Students t-test. For label free quantitation, all spectra identified as matches to peptides of a given protein were reported, and the number of spectra (Peptide Spectral Matches, PSMs) exported to Excel and used for label free quantitation of protein abundance in the samples. Relative abundance indexes were calculated as ratios of the PSMs vs. the molecular weight of the polypeptide.

QUANTIFICATION AND STATISTICAL ANALYSIS

Quantification of axon regeneration: images of optic nerve axons, traced with cholera-toxin-beta (CTB), were processed using Zeiss ZEN 3.5 software (blue edition) and stored as TIFF files. The images were imported into FIJI processing software Version 2.1.0, cropped from injury site (0 mm) to 2 mm distal to the injury site. Images were converted to 8-bit and saved as a TIFF files. Images were saved into the working directory for automated optic nerve axon counting code to be executed. The code generated for axon counting is made publicly available through Github: https://github.com/mcfinner/MF_Axon_Count_1.0. Briefly, Images are read into R Version 4.1.2, thresholded and masked for signal intensity, and cropped into intervals of 0-to-2mm in four intervals. Objects in the

image are then identified using the EBImage R package 4.39.0 (Pau G et al., 2010) colored, and object features are computed - such as surface area. These variables are used to determine the number of ''axon-like'' objects in each interval for objects that have a surface area >400 units. The number of axons per section is then used to calculate the axons per nerve at each interval and exported into a final excel output file. High fluorescent intensity signal in the first interval (0-to-0.5 mm) may cause an inaccurate count, and should be compared to the second interval for the most accurate number of axons in the first 0-to-1.0 mm.

Statistics

Data are presented as mean ± SEM. Statistical analysis was performed in GraphPad Prism (v9) using paired or unpaired two-tailed Student's *t* test, or one-way or two-way ANOVA with correction for multiple comparisons with Tukey's post-hoc test, as indicated in the figure legends. A *p value<0.05 was considered significant. **$p < 0.01$, ***$p < 0.001$, and ****$p < 0.0001$. Data acquisition and analysis were carried out by individuals blinded to experimental groups.

Cell Reports, Volume *43*

Supplemental information

Neutrophil-inflicted vasculature damage suppresses immune-mediated optic nerve regeneration

Ryan Passino, Matthew C. Finneran, Hannah Hafner, Qian Feng, Lucas D. Huffman, Xiao-Feng Zhao, Craig N. Johnson, Riki Kawaguchi, Juan A. Oses-Prieto, Alma L. Burlingame, Daniel H. Geschwind, Larry I. Benowitz, and Roman J. Giger

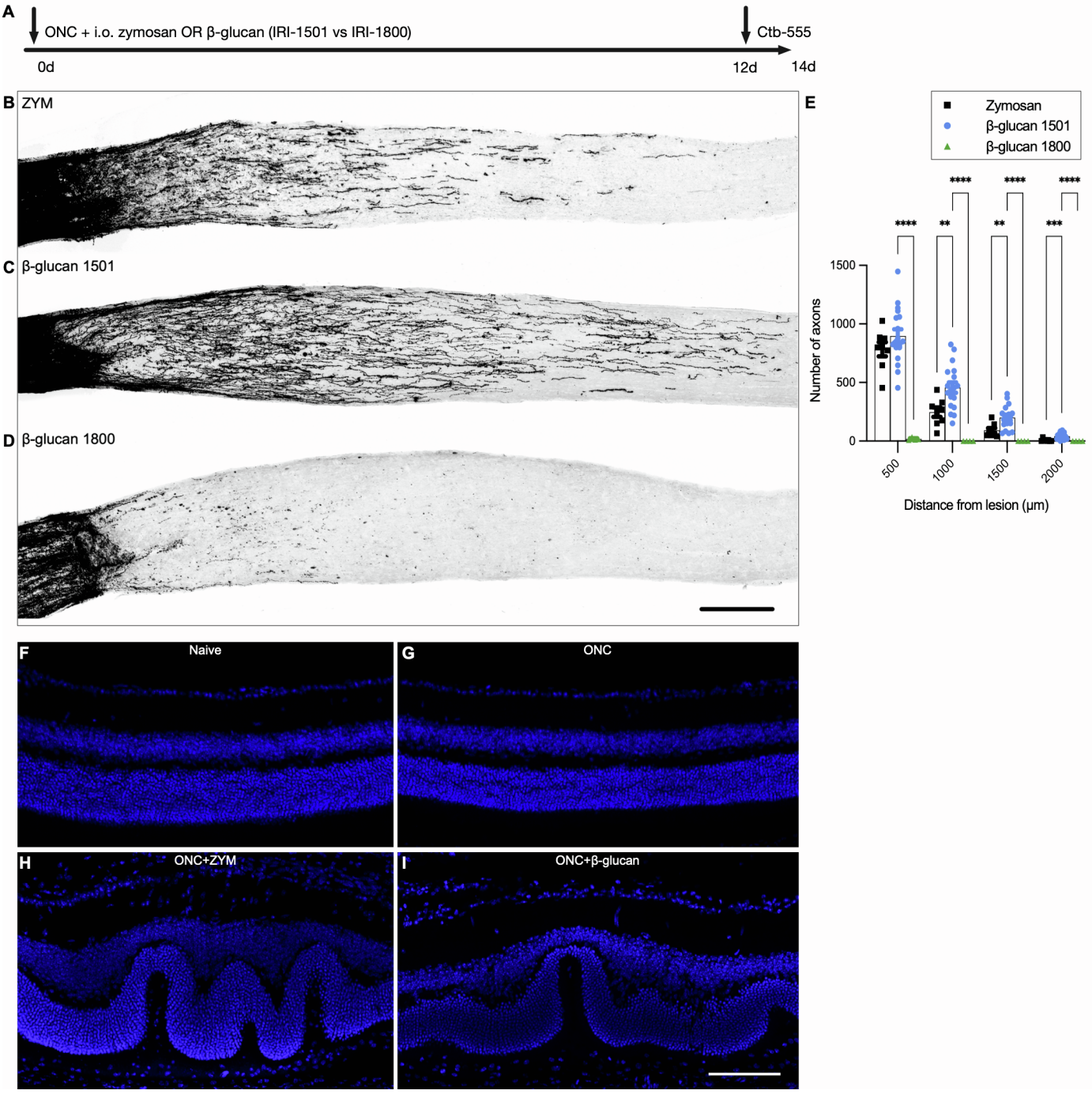

Supplementary Figure 1: Particulate β-glucan is superior to zymosan and soluble β-glucan in promoting RGC axon regeneration (Related to Figure 1).

(**A**) Experimental timeline for assessing optic nerve axon regeneration following i.o. zymosan and different β-glucan preparations. (**B-D**) Longitudinal optic nerve sections with CTB traced axons at 14dpc with i.o. (**B**) zymosan, (**C**) particulate β(1,3)(1,6)-glucan [IRI-1501], and (**D**) soluble β(1,3)(1,6)-glucan [IRI1800]. (**E**) Quantification of regenerated axons. Y-axis, of number axons per nerve. X-axis distance from nerve crush site. Number of regenerated axons at 500, 1000, 1500, and 2000 μm past the crush site is shown. Zymosan (n= 8 nerves); particulate β-glucan (n= 18 nerves); soluble β-glucan (n= 4 nerves). Results are presented as mean ± SEM. Data were analyzed with 2-way ANOVA followed by Tukey's multiple comparisons test. ** $p \leq 0.01$; *** $p \leq 0.001$; **** $p \leq 0.0001$. Scale bar, 200μm. (**F-I**) Retinal cross-sections labeled with the nuclear dye DAPI, showing the retinal layers of (**F**) naïve mice, (**G**) 3dpc with i.o. PBS, (**H**) 3dpc with i.o. zymosan, and (**I**) 3dpc with β-glucan. Scale bar, 100μm.

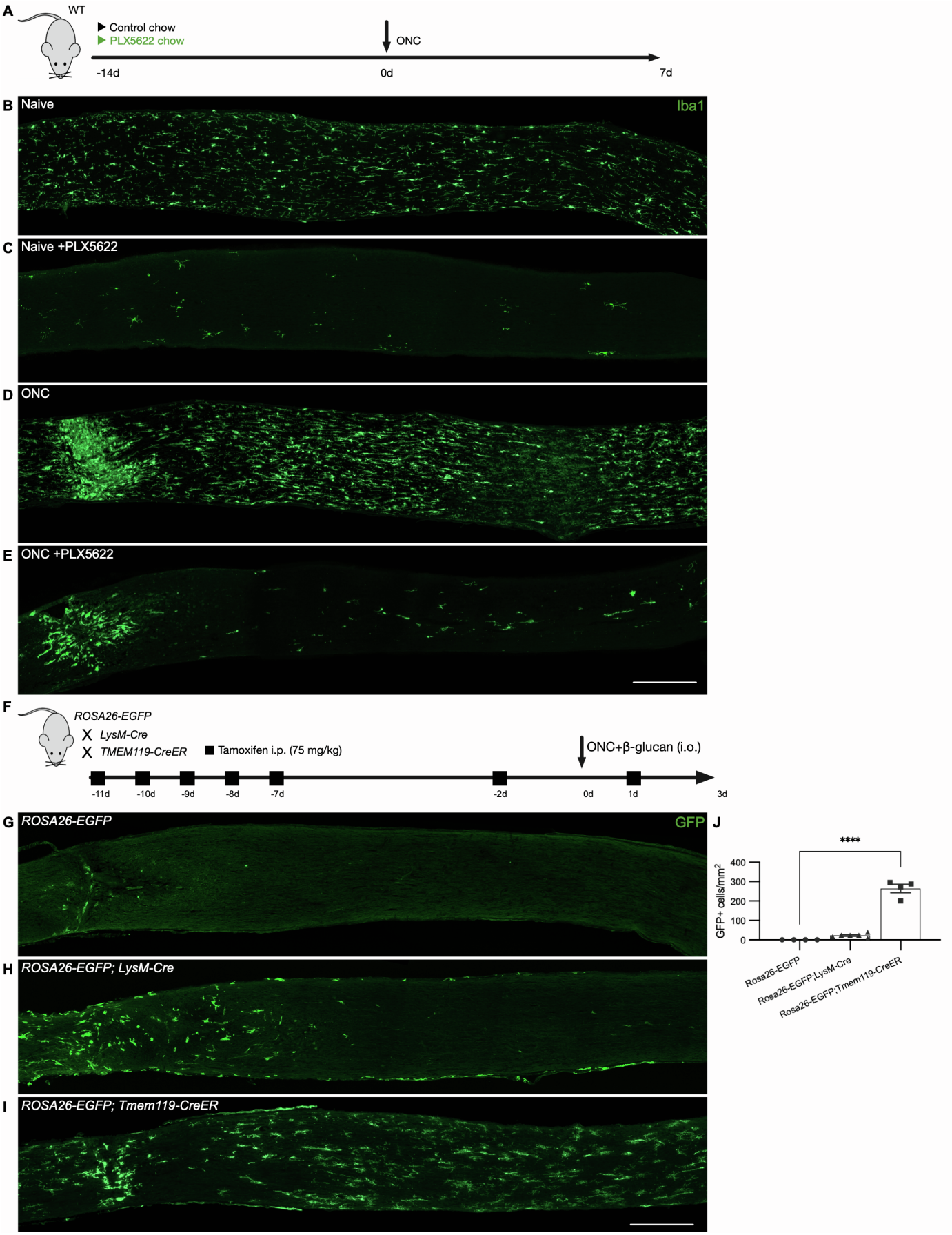
A
WT
Control chow
PLX5622 chow
ONC
-14d
0d
7d
B
Naive
Iba1
C
Naive +PLX5622
D
ONC
E
ONC +PLX5622
F
ROSA26-EGFP
X LysM-Cre
X TMEM119-CreER
Tamoxifen i.p. (75 mg/kg)
ONC+β-glucan (i.o.)
-11d
-10d
-9d
-8d
-7d
-2d
0d
1d
3d
G
ROSA26-EGFP
GFP
H
ROSA26-EGFP; LysM-Cre
I
ROSA26-EGFP; Tmem119-CreER
J
****
GFP+ cells/mm2
400
300
200
100
0
Rosa26-EGFP
Rosa26-EGFP;LysM-Cre
Rosa26-EGFP;Tmem119-CreER

Supplementary Figure 2: Assessment of cre recombination efficiency in *Tmem119-CreER* and *LysM-Cre* mice (Related to Figure 1).

(**A**) Experimental timeline for assessing optic nerve microglia ablation efficiency with PLX5622 chow vs control chow. (**B-E**) Optic nerve sections from (**B**) naïve controls, (**C**) naïve with PLX5622, (**D**) ONC controls, and (**E**) ONC with PLX5622. (**F**) Experimental timeline for assessing recombination efficiency of *Tmem119-CreER* and *LysM-Cre* crossed with *ROSA26-EGFP* reporter mice at 3dpc and i.o. β-glucan. (**G**) Optic nerve sections of *ROSA26-EGFP* mice, (**H**) *LysM-Cre;ROSA26-EGFP* mice, and (**I**) *Tmem119-CreER;ROSA26-EGFP* mice. Scale bar, 200 μm. (**J**) Recombination efficiency represents the number of recombined (GFP+) cells per mm^2 at 500 μm distal to the crush site. n= 3 for *ROSA26-EGFP*, n= 6 for *LysM-Cre;ROSA26-EGFP*, and n= 4 for *Tmem119-CreER;ROSA26-EGFP*. Results are presented as mean ± SEM. Data were analyzed with 1-way ANOVA followed by Tukey's multiple comparisons test. **** $p \leq 0.0001$.

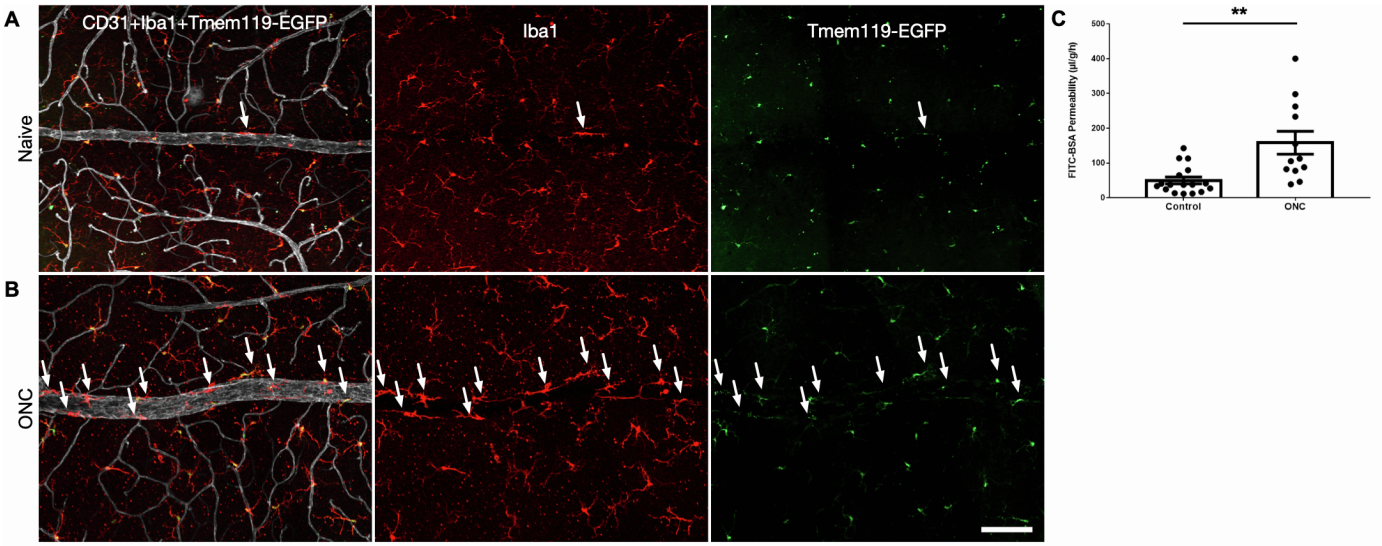

Supplementary Figure 3: Perivascular microglia respond to optic nerve injury and protect the BRB (Related to Figure 2).

(**A-B**) Retinal flat mounts of naïve and 1dpc *Tmem119-EGFP* reporter mice co-labeled with anti-CD31 (white) and anti-Iba1 (red). Arrowheads label perivascular microglia that respond to ONC. (**C**) Quantification of BRB leakiness at 3dpc, as assessed by FITC-BSA accumulation in naïve retinas (n= 17) and injured retinas (n= 12). FITC-BSA tail vein injection was carried out at 2dpc and permeability through the BRB quantified after 24h. Student's t test, ** p-value (0.0011).

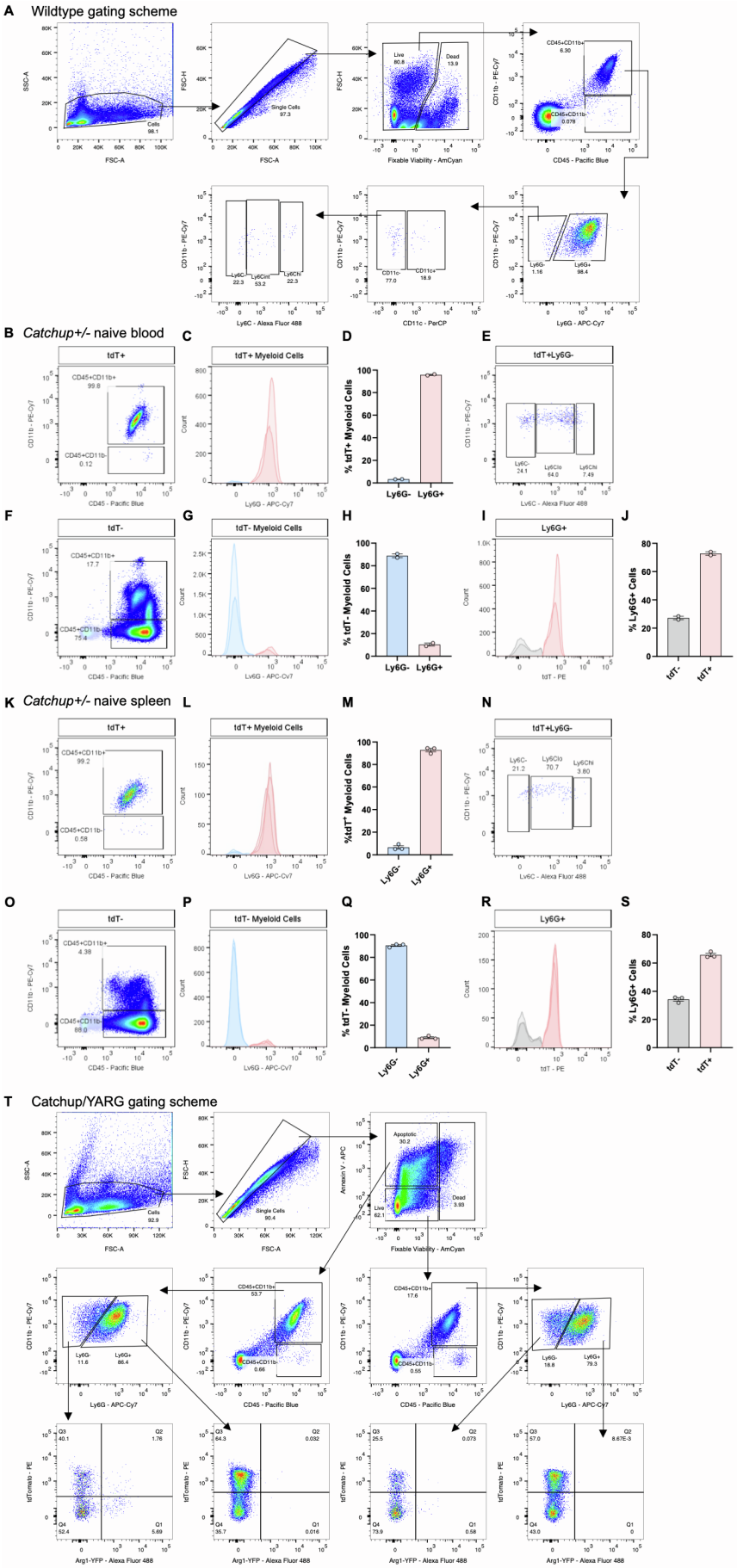
A Wildtype gating scheme
B Catchup+/- naive blood
C
D
E
F
G
H
I
J
K Catchup+/- naive spleen
L
M
N
O
P
Q
R
S
T Catchup/YARG gating scheme
tdT+
tdT+ Myeloid Cells
tdT+Ly6G-
tdT-
tdT- Myeloid Cells
Ly6G+
% tdT+ Myeloid Cells
% tdT- Myeloid Cells
% Ly6G+ Cells
%tdT+ Myeloid Cells
Ly6G-
Ly6G+
tdT-
tdT+

Supplementary Figure 4: Gating Strategy for flow cytometry (Related to Figure 3).

(**A**) For identification of immune cell population in the vitreous, retina, and spleen cell suspensions were prepared and gated with forward scatter (FSC-A) and side scatter (SSC-A) to exclude debris. Next, cells were gated with forward scatter height (FSC-H) and FSC-A to find single cells and to exclude doublets. Live cells were isolated by negative staining for fixed viability dye. Leukocytes were analyzed as follows: lymphocytes were isolated as $CD45^+$, $CD11b^-$. Myeloid cells ($CD45^+$, $CD11b^+$) were further separated into $Ly6G^+$ granulocytes. The remaining cells ($CD45^+$, $CD11b^+$, $Ly6G^-$) were characterized as dendritic cells ($CD45^+$, $CD11b^+$, $CD11c^+$, $Ly6G^-$), and Mo/Mac ($CD45^+$, $CD11b^+$, $CD11c^-$, $Ly6G^-$) and further analyzed for Ly6C surface expression. (**B-E**) Blood and spleen of *Catchup+/-* mice were analyzed as described under (**A**). The percent of tdtomato (tdT)+ cells in the Ly6G- and Ly6G+ myeloid population was quantified (n= 2 mice). (**F-J**) In addition, the fraction of Ly6G+ cells in the tdT- myeloid cell population was determined. (**K-S**) A similar gaiting strategy was used to determine the fraction of tdT+ GC in the spleen and tdT- GC in the spleen (n= 3). (**T**) For identification of GC that also express Arg1, we used *Catchup+/-;Arg1-YFP+/-* mice following the same gating strategy as for wildtype mice with the following modifications. Dead cells were identified by staining for the fixed viability dye, apoptotic cells were identified by surface binding of Annexin V, and live cells were identified as double negative cells. GC were identified as ($CD45^+$, $CD11b^+$, $Ly6G^+$) and analyzed for expression of tdT and YFP.

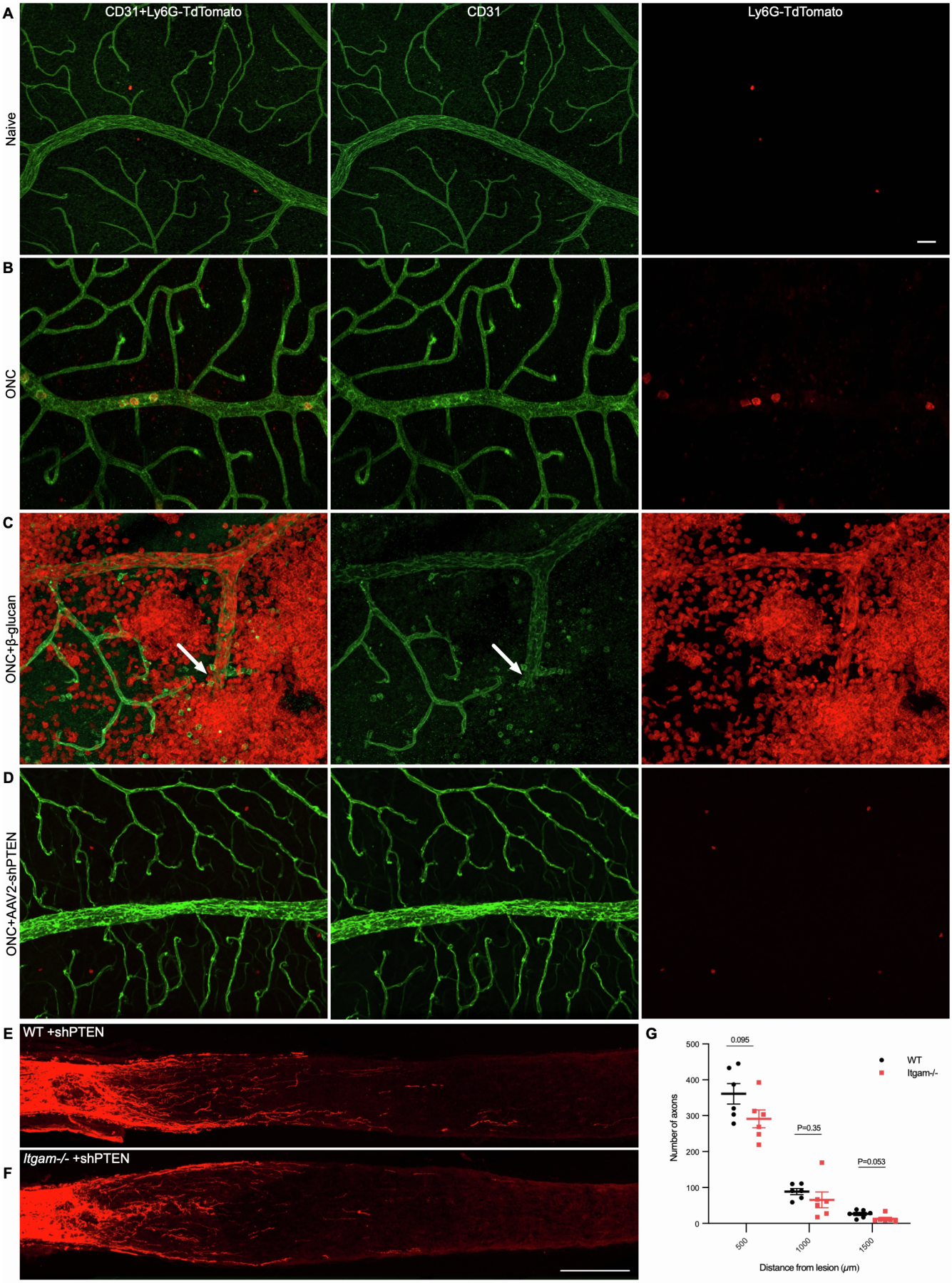
A
CD31+Ly6G-TdTomato
CD31
Ly6G-TdTomato
Naive
B
ONC
C
ONC+β-glucan
D
ONC+AAV2-shPTEN
E
WT +shPTEN
F
Itgam-/- +shPTEN
G
0.095
P=0.35
P=0.053
WT
Itgam-/-
Number of axons
500
400
300
200
100
0
500
1000
1500
Distance from lesion (μm)

Supplementary Figure 5: Neutrophils in the retinal vasculature of naïve mice and following ONC (Related to Figure 3).

(**A-C**) Retinal flat mounts of *Catchup+/-* reporter mice from (**A**) naïve mice, (**B**) ONC at 1dpc with i.o. PBS, (**C**) ONC at 1dpc with i.o. β-glucan, and (**D**) ONC at 1dpc of mice with i.o. AAV2-shPTEN 14d prior to ONC. The retinal vasculature (green) is labeled with anti-CD31. Arrow in C points to a damaged blood vessel. Scale bar, 50μm. (**E**) Longitudinal optic nerve sections with CTB traced axons at 14dpc with AAV2-shPTEN in (**E**) WT (n= 4) and (**F**) *Itgam-/-* (n= 4) mice. (**G**) Quantification of regenerated RGC axons. Y-axis, number of axons per nerve. X-axis distance from nerve crush site. The number of regenerated axons at 500, 1000, 1500 μm past the crush site is shown. Results are presented as mean ± SEM. Data were analyzed using Student's t-test. None of the comparisons showed a p-value ≤ 0.05.

A

scRNA-seq datasets	Number of cells sequenced (analyzed)	Technical replicates	Median counts per cell	Median genes per cell	Number of reads	Sequencing saturation
WT	18,943 (16,666)	2	5,303	1,875	1.69B	81.75%
Itgam-/-	19,419 (16,493)	2	5,427	1,970	1.23B	73.26%

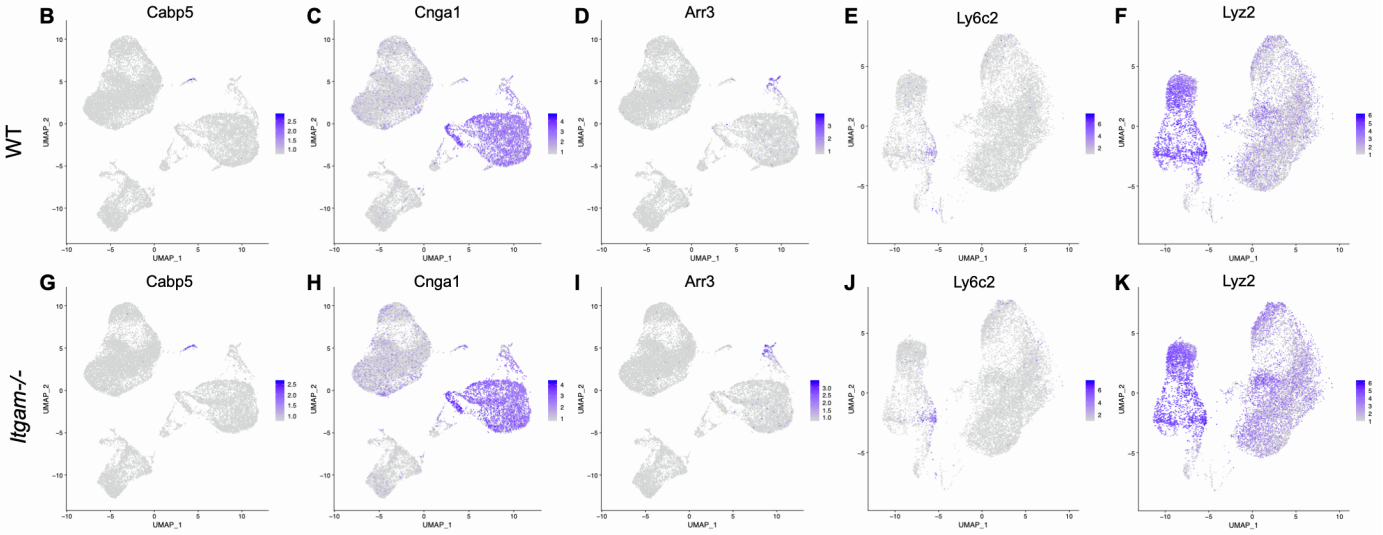

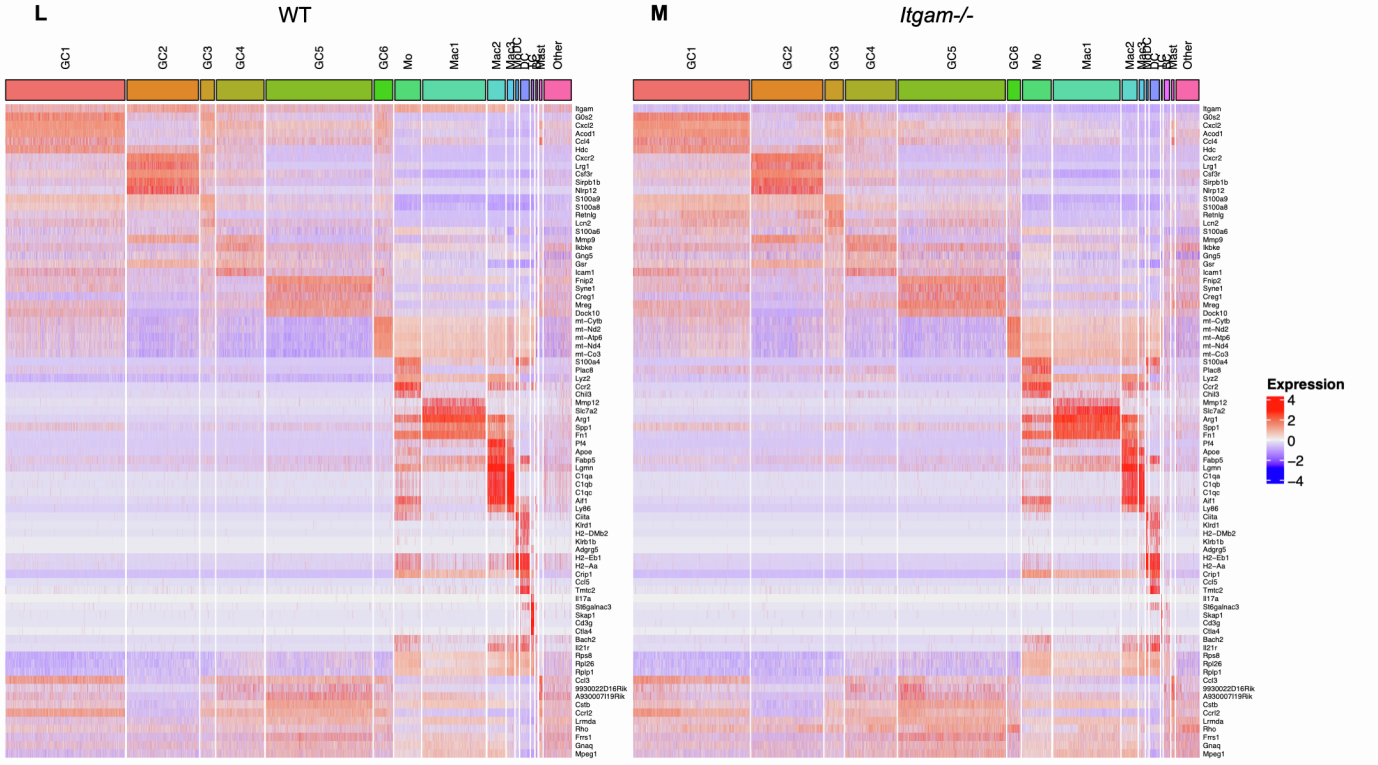

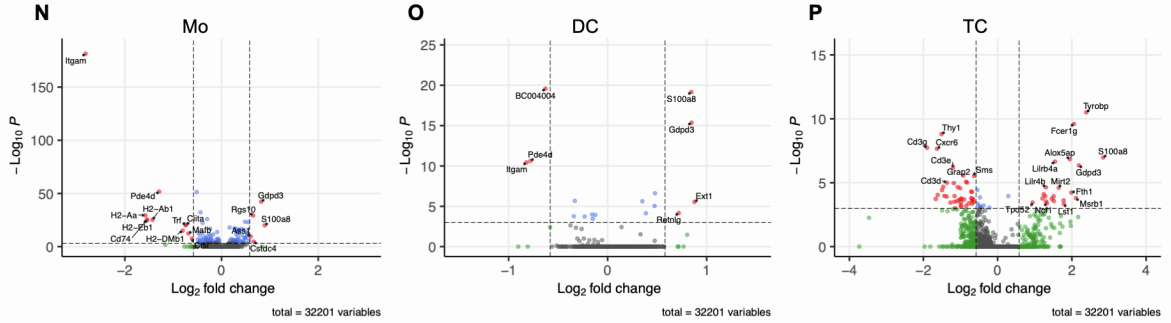

Supplementary Figure 6: Quality test of scRNAseq datasets and identification of immune cells in the vitreous of wildtype and *Itgam-/-* mice following i.o. β-glucan (Related to Figure 5).

(**A**) Table with technical specifications of scRNAseq datasets of anti-CD45 MACS-sorted leukocytes prepared from WT and *Itgam-/-* vitreous and retina 3dpc plus β-glucan. Feature plots of (**B-F**) WT and (**G-K**) *Itgam-/-* datasets reveal clusters with non-immune cells, including (**B, G)** bipolar cells expressing *Cabp5*, (**C, H**) rod photoreceptors expressing *Cnga1*, and (**D, I**) cone photoreceptors expressing *Arr3*. Non-immune cells were removed *in silico* and the remaining cells analyzed for the presence of (**E, J**) monocytes (*Ly6c2*), and (**F, K**) Macrophages were identified in feature plots by their preferential expression of *Lyz2*. (**L, M**) heatmaps of WT and *Itgam-/-* leukocytes showing cluster enriched gene products. (**N, O, P**) Volcano plot of monocytes (Mo), dendritic cells (DC), and T cells (TC) showing differentially expressed gene products between WT and *Itgam-/-* cells. Normalized signal on the y-axis shows the -log10 p-value and the x-axis the log2-fold change. Abbreviations, GC (granulocytes), Mo (monocytes), Mac (macrophages), MoDC (monocyte-derived macrophages), DC (dendritic cells), TC (T cells), BC (B cells), Mast (mast cells), other (technical artifacts).

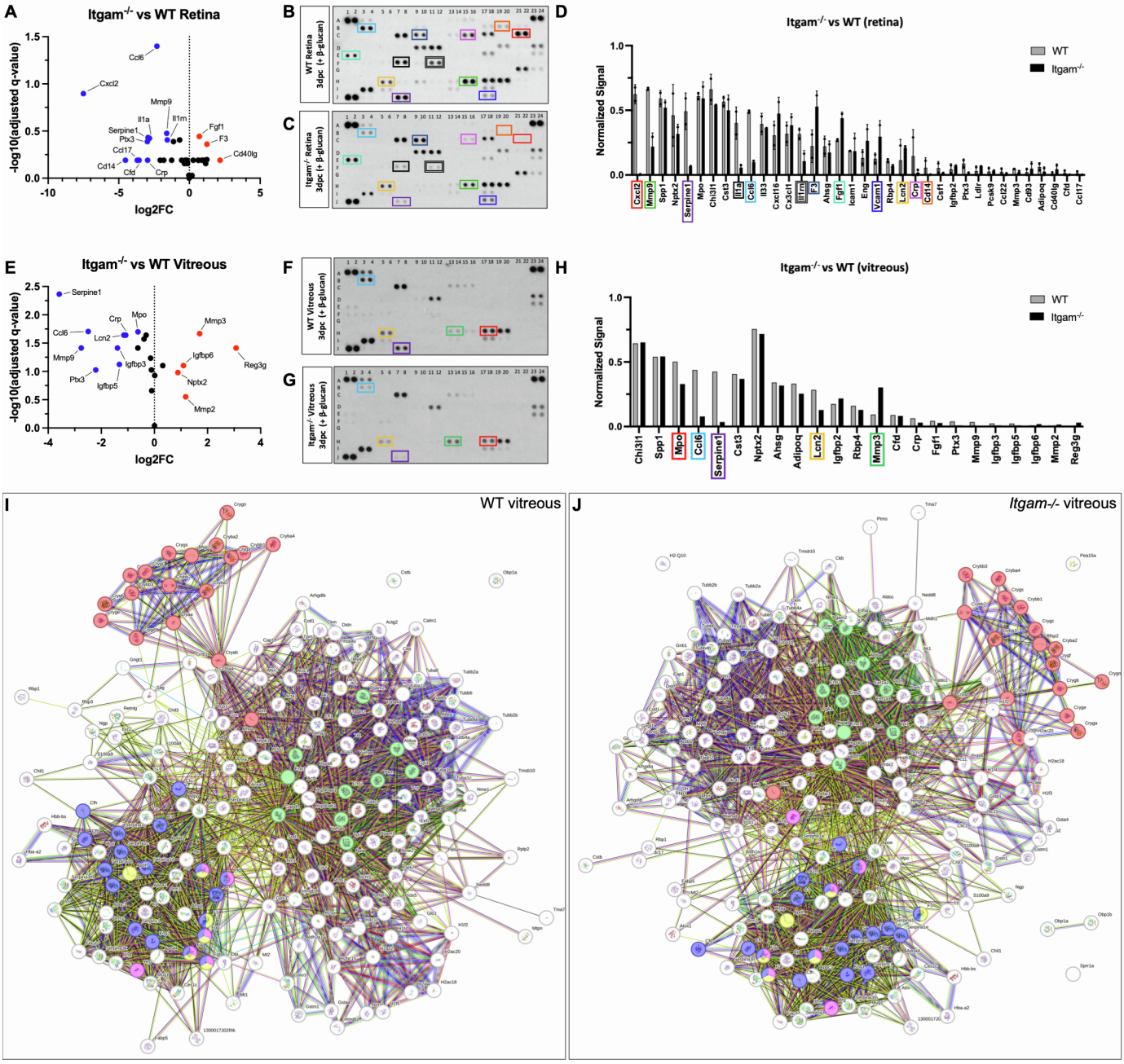

Supplementary Figure 7: Ocular proteome of WT and *Itgam-/-* mice following ONC and i.o. β-glucan (Related to Figure 6).

(**A-D**) Representative ELISA membranes probed with retinal lysates prepared at 3dpc and i.o. β-glucan of (**B**) WT (n = 2) and (**C**) *Itgam-/-* (n= 2) mice. (**A**) Volcano plot showing differentially abundant proteins in *Itgam-/-* retina compared to WT retina. (**D**) List of most abundant proteins. For quantification, ELISA signals were normalized to reference spots shown at coordinates (A1, A2), (A23, A24), and (J1, J2). (**E-H**) Representative ELISA membranes probed with vitreal proteins prepared at 3dpc and i.o. β-glucan of (**F**) WT (n = 1) and (**G**) *Itgam-/-* (n= 1) mice. (**E**) Volcano plot showing differentially abundant proteins in *Itgam-/-* retina compared to WT retina. (**H**) List of most abundant proteins. For quantification, ELISA signals were normalized to reference spots shown at coordinates. The coordinates for proteins that can be detected by multiplex ELISA are as follows: (A1, A2) reference spots, (A3, A4) Adiponectin [*Adipoq*], (A5, A6) Amphiregulin [*Areg*], (A7, A8) Angiopoientin-1 [*Angpt1*], (A9, A10) Angiopoientin-2 [*Angpt2*], (A11, A12) Angiopoientin-like 3 [*Angptl3*], (A13, A14) BAFF [*Tnfrsf13b*], (A15, A16) C1qR1 [*Cd93*], (A17, A18) CCL2 [*Ccl2*], (A19, A20) CCL3 [*Ccl3*], (A21, A22) CCL5 [*Ccl5*], (A23, A24) Reference spots, (B3, B4) CCL6 [*Ccl6*], (B5, B6) CCL11 [*Ccl11*], (B7, B8)

CCL12 [*Ccl12*], (B9, B10) CCL17 [*Ccl17*], (B11, B12) CCL19 [*Ccl19*], (B13, B14) CCL20 [*Ccl20*], (B15, B16) CCL21 [*Ccl21*], (B17, B18) CCL22 [*Ccl22*], (B19, B20) CD14 [*Cd14*], (B21, B22) CD40 [*Cd40*], (C3, C4) CD160 [*Cd160*], (C5, C6) Chemerin [*Rarres2*], (C7, C8) Chitinase 3-like 1 [*Chil3*], (C9, C10) Coagulation Factor III [*F3*], (C11, C12) Complement Component C5 [*C5*], (C13, C14) Complement Factor D [*Cfd*], (C15, C16) C-Reactive Protein [*Crp*], (C17, C18) CX3CL1 [*Cx3cl1*], (C19, C20) CXCL1 [*Cxcl1*], (C21, C22) CXCL2 [*Cxcl2*], (D1, D2) CXCL9 [*Cxcl9*], (D3, D4) CXCL10 [*Cxcl10*], (D5, D6) CXCL11 [*Cxcl11*], (D7, D8) CXCL13 [*Cxcl13*], (D9, D10) CXCL16 [*Cxcl16*], (D11, D12) Cystatin C [*Cst3*], (D13, D14) DKK-1 [*Dkk1*], (D15, D16) DPPIV [*Dpp4*], (D17, D18) EGF [*Egf*], (D19, D20) Endoglin [*Eng*], (D21, D22) Endostatin [*Col18a1*], (D23, D24) Fetuin A [*Ahsg*], (E1, E2) FGF acidic [*Fgf1*], (E3, E4) FGF-21 [*Fgf21*], (E5, E6) Flt-3 Ligand [*Flt3l*], (E7, E8) Gas 6 [*Gas6*], (E9, E10) G-CSF [*Csf3*], (E11, E12) GDF-15 [*Gdf15*], (E13, E14) GM-CSF [*Csf2*], (E15, E16) HGF [*Hgf*], (E17, E18) ICAM-1 [*Icam1*], (E19, E20) IFN-gamma [*Ifng*], (E21, E22) IGFBP-1 [*Igfbp1*], (E23, E24) IGFBP-2 [*Igfbp2*], (F1, F2) IGFBP-3 [*Igfbp3*], (F3, F4) IGFBP-5 [*Igfbp5*], (F5, F6) IGFBP-6 [*Igfbp6*], (F7, F8) IL-1alpha [*Il1a*], (F9, F10) IL-1Beta [*Il1b*], (F11, F12) IL-1ra [*Il1rn*], (F13, F14) IL-2 [*Il2*], (F15, F16) IL-3 [*Il3*], (F17, F18) IL-4 [*Il4*], (F19, F20) IL-5 [*Il5*], (F21, F22) IL-6 [*Il6*], (F23, F24) IL-7 [*Il7*], (G1, G2) IL-10 [*Il10*], (G3, G4) IL-11 [*Il11*], (G5, G6) IL-12 p40 [*Il12*], (G7, G8) IL-13 [*Il13*], (G9, G10) IL-15 [*Il15*], (G11, G12) IL-17A [*Il17a*], (G13, G14) IL-22 [*Il22*], (G15, G16) IL-23 [*Il23*], (G17, G18) IL-27 p28 [*Il27*], (G19, G20) IL-28 [*Ifnl3*], (G21, G22) IL-33 [*Il33*], (G23, G24) LDL R [*Ldlr*], (H1, H2) Leptin [*Lep*], (H3, H4) LIF [*Lif*], (H5, H6) Lipocalin-2 [*Lcn2*], (H7, H8) LIX [*Cxcl5*], (H9, H10) M-CSF [*Csf1*], (H11, H12) MMP-2 [*Mmp2*], (H13, H14) MMP-3 [*Mmp3*], (H15, H16) MMP-9 [*Mmp9*], (H17, H18) Myeloperoxidase [*Mpo*], (H19, H20) Osteopontin [*Spp1*], (H21, H22) Osteoprotegerin [*Tnfrsf11b*], (H23, H24) PD-ECGF [*Tymp*], (I1, I2) PDGF-BB [*Pdgfb*], (I3, I4) Pentraxin 2 [*Nptx2*], (I5, I6) Pentraxin 3 [*Ptx3*], (I7, I8) Periostin [*Postn*], (I9, I10) Pref-1 [*Dlk1*], (I11, I12) Proliferin [*Prl2c2*], (I13, I14) Proprotein Convertase 9 [*Pcsk9*], (I15, I16) RAGE [*Ager*], (I17, I18) RBP4 [*Rbp4*], (I19, I20) Reg3G [*Reg3g*], (I21, I22) Resistin [*Retn*], (J1, J2) Reference spots, (J3, J4) E-Selectin [*Sele*], (J5, J6) P-Selectin [*Selp*], (J7, J8) Serpin E1 [*Serpine1*], (J9, J10) Serpin F1 [*Serpinf1*], (J11, J12) Thrombopoietin [*Thpo*], (J13, J14) TIM-1 [*Havcr1*], (J15, J16) TNF-alpha [*Tnf*], (J17, J18) VCAM-1 [*Vcam1*], (J19, J20) VEGF [*Vegf*], (J21, J22) WISP-1 [*Ccn4*], (J23, J24) negative control. (**I, J**) String.db analysis of vitreal proteome of WT and *Itgam-/-* mice at 3dpc plus i.o. β-glucan. Identified pathways include (**I**) **Red**: lens development (FDR 2.24e-15); **Purple**: complement and coagulation cascades (FDR 1.25e-15); **Green**: canonical glycolysis (FDR 1.00e-11); **Yellow**: blood coagulation, fibrin clot formation (FDR 9.37e-06); **Pink**: fibrinolysis (FDR 2.54e-06). (**J**) **Red**: lens development (FDR 3.25e-15); **Purple**: complement and coagulation cascades (FDR 7.76e-17); **Green**: canonical glycolysis (FDR 9.48e-12); **Yellow**: blood coagulation, fibrin clot formation (FDR 1.04e-05); **Pink**: fibrinolysis (FDR 1.01e-07);